Nano Energy 159 (2026) 112487

Contents lists available at ScienceDirect

Nano Energy

journal homepage: www.elsevier.com/locate/nanoen

Full paper

Stabilizing Li- and Mn-rich layered cathodes through oxygen-redox-coupled interphase transformation

Hyunjin Jang [a,c,1], Seyeop Oh [a,c,1], Hoseok Lee [b,c], Hyunji Kweon [a,c], Bonyoung Ku [a,c], Myungeun Choi [a,c], Jihoe Lee [a,c], Jinho Ahn [a,c], Hyunyoung Park [a,c], Myeong Hwan Lee [d], Hyun-seung Kim [a,b,*], Jongsoon Kim [a,b,c,*]

[a] Department of Energy Science, Sungkyunkwan University, Suwon, 16419, Republic of Korea
[b] Department of Future Energy Engineering, Sungkyunkwan University, Suwon, 16419, Republic of Korea
[c] SKKU Institute of Energy Science and Technology (SIEST), Sungkyunkwan University, Suwon, 16419, Republic of Korea
[d] Advanced Energy Materials Research Center, Korea Research Institute of Chemical Technology (KRICT), 141, Gajeongro, Yuseong, Daejeon, 34114, Republic of Korea

ARTICLE INFO

Keywords:
Cathode materials
First-principles calculation
Li-ion batteries
Li- and Mn-rich layered oxides

ABSTRACT

Li- and Mn-rich layered oxides (LMRs) offer high capacity through transition-metal and oxygen redox but undergo irreversible oxygen loss and surface degradation during high-voltage operation. Here, we investigate an oxygen-redox-coupled cathode–electrolyte interphase (ORC-CEI) strategy based on the proposed interaction of SO_3-containing moieties with reactive surface oxygen, using 1,4-butane sultone (BS) as the precursor. Voltage-resolved XPS and ToF-SIMS reveal transformation of the BS-derived interphase toward sulfate-like environments. Calculations using a nominal Ni^{4+}/Mn^{4+} surface reference model show that the proposed S–O anchoring locally reduces oxygen-hole density and raises the energy required to remove the participating lattice oxygen. Complementary measurements show reduced O_2 evolution and mitigated surface reconstruction. Following formation to 4.7 V, the modified $Li_{1.2}Ni_{0.2}Mn_{0.6}O_2$ cathode retains 79% of its capacity after 100 cycles over 2.3–4.5 V at 125 mA g^{-1}, compared with 57% for the baseline electrode. With repeated cycling to 4.7 V, the corresponding retention is 67% after 70 cycles versus 37%. These results support the proposed connection between interphase transformation and local surface-oxygen stabilization.

1. Introduction

Lithium-ion batteries (LIBs) have become the dominant energy storage technology for portable electronics, electric vehicles, and large-scale energy storage systems owing to their high energy density and long cycle life [1]. As the demand for electrified transportation and grid-scale energy storage continues to increase, the development of next-generation cathode materials capable of delivering higher energy density has become increasingly important [2]. In particular, achieving high reversible capacity while maintaining structural and interfacial stability under high-voltage operation remains a central challenge for advanced LIB systems.

Among various cathode candidates, Co-free Li- and Mn-rich layered oxides (LMRs) have attracted considerable attention because they can deliver capacities exceeding 250 mAh g^{-1} through the combined participation of transition-metal (TM) and lattice oxygen redox processes during high-voltage charging [3,4]. This dual-redox mechanism enables significantly higher energy densities than those of conventional layered oxide cathodes. However, despite these advantages, LMR cathodes suffer from severe voltage decay, structural degradation, and progressive deterioration of the cathode–electrolyte interface during cycling, which remain major obstacles for their practical implementation [5,6].

The instability of LMR cathodes is closely associated with oxygen-active surface environments generated during high-voltage operation. When lithium extraction exceeds the TM-based redox limit, lattice oxygen can be partially oxidized to O^- species [7,8]. These oxygen radicals are thermodynamically unstable and tend to undergo O–O dimerization, which may ultimately lead to molecular oxygen release from the lattice [9,10]. The formation of O–O dimers and oxygen evolution induces

* Corresponding authors at: Department of Energy Science, Sungkyunkwan University, Suwon 16419, Republic of Korea.
E-mail addresses: hskim0113@skku.edu (H.-s. Kim), jongsoonkim@skku.edu (J. Kim).
[1] These authors contributed equally to this work

https://doi.org/10.1016/j.nanoen.2026.112487
Received 5 August 2026; Received in revised form 1 October 2026; Accepted 8 October 2026
Available online 9 October 2026
2211-2855/© 2026 Elsevier Ltd. All rights are reserved, including those for text and data mining, AI training, and similar technologies.

irreversible surface reconstruction from layered to spinel- or rock-salt-like phases [11–13]. In addition, oxygen-active surfaces significantly accelerate electrolyte oxidation and parasitic interfacial reactions, resulting in rapid impedance growth and pronounced voltage decay during cycling [14–16].

To mitigate these degradation pathways, extensive efforts have been devoted to stabilizing the cathode–electrolyte interface (CEI), including surface coatings [17–19], compositional modification [20,21], and electrolyte additive engineering [22,23]. Among these approaches, electrolyte additives represent a particularly effective strategy for regulating interfacial reactions [24,25]. However, most conventional additives were originally developed for layered oxide cathodes whose electrochemical behavior is governed primarily by TM-based redox reactions [26,27]. In these systems, additive decomposition is typically tailored to suppress electrolyte oxidation at high potentials associated with TM-based redox processes [28–30].

In LMR cathodes, oxygen participation in charge compensation introduces an additional requirement for interphase design: stabilization of reactive oxygen sites generated during high-voltage charging [31–33]. Conventional sulfur-containing CEIs are commonly discussed in terms of their protective interphase properties. However, the presence of sulfate-like species alone does not establish chemical stabilization of the oxidized oxygen sites of the cathode. The interaction between an interphase-forming species and reactive surface oxygen therefore warrants consideration alongside the composition of the resulting protective film.

Recent studies have explored oxygen-reactivity-based interfacial engineering, including nucleophilic oxygen-engineered dual-gradient CEIs and electrophilic electrolyte formulations for high-voltage stabilization [34,35]. These studies provide precedents for using oxygen reactivity to regulate cathode–electrolyte interactions. Our previous study demonstrated that 1,4-butane sultone (BS) stabilizes the CEI and improves high-voltage cycling of Co-free $LiNi_{0.75}Mn_{0.25}O_2$ (NMX), with its relatively low HOMO level considered in relation to high-voltage compatibility [24]. Building on this work, the present study examines the chemical functionality of an SO_3-containing moiety toward reactive surface oxygen in oxygen-redox-active LMR cathodes.

We propose that BS-derived organosulfonate moieties can participate in interfacial bond reorganization involving S–O bonding with cathode surface oxygen, producing a surface-bound sulfate-like environment. Within this model, the SO_3-containing moiety provides the precursor functionality, whereas the sulfate-like environment describes the resulting surface-bonded configuration. The proposed protective function arises from local electronic passivation of the participating oxygen through this interaction. BS serves as the molecular precursor used to investigate this concept. Voltage-resolved interphase characterization, gas-evolution measurements, structural analyses, and calculations are combined to evaluate the proposed connection between interphase transformation and suppression of irreversible surface degradation.

Here, we investigate this oxygen-redox-coupled cathode–electrolyte interphase (ORC-CEI) strategy using Co-free $Li_{1.2}Ni_{0.2}Mn_{0.6}O_2$ (LNM) and a BS-containing electrolyte. The resulting system, denoted as LNM@ORC-CEI, is examined in terms of voltage-dependent transformation of SO_3-containing interphase species and the proposed local stabilization of reactive surface oxygen through S–O bonding. Electrochemical measurements show an initial Coulombic efficiency (ICE) of $82.16 \pm 0.24\%$ for LNM@ORC-CEI, compared with $79.72 \pm 0.09\%$ for the bare LNM reference cathode (B-LNM; mean $\pm$ sample standard deviation, $n = 3$). Following an initial formation cycle to 4.7 V, LNM@ORC-CEI retains 79% of its initial capacity after 100 cycles over 2.3–4.5 V at 125 mA g^{-1}, compared with 57% for B-LNM. In addition, the ORC-CEI effectively suppresses voltage decay, exhibiting a voltage drop of 1.3 mV per cycle compared with 3.2 mV for B-LNM.

Structural and spectroscopic analyses further support an association between the improved electrochemical stability and regulation of oxygen-redox-driven surface reactions by the ORC-CEI. The interphase suppresses irreversible structural degradation, reduces O_2 evolution and parasitic electrolyte oxidation at high states of charge, and is associated with more reversible evolution of the TM–O electronic structure during cycling. In addition, first-principles calculations indicate local electronic passivation of the anchored surface oxygen within the modeled configuration. As a result, the ORC-CEI significantly enhances the structural integrity and electrochemical durability of LMR cathodes under high-voltage operation.

2. Results and discussion

2.1. Proposed surface-oxygen anchoring of BS-derived species in LMR cathodes

First-principles calculations were performed to examine how the proposed S–O anchoring interaction modifies reactive surface oxygen, with the Heyd–Scuseria–Ernzerhof (HSE06) hybrid functional used for projected density-of-states analysis [36]. A simplified $Li_{12}Ni_3Mn_{12}O_{36}$ surface model was employed to approximate the nominal Ni^{4+}/Mn^{4+} environment associated with partially delithiated $Li_{0.8}Ni_{0.2}Mn_{0.6}O_2$. Under formal charge counting, $Li_{0.8}Ni_{0.2}Mn_{0.6}O_2$ corresponds to the extraction of 0.4 Li from $Li_{1.2}Ni_{0.2}Mn_{0.6}O_2$ through Ni^{2+}-to-Ni^{4+} oxidation with Mn remaining nominally tetravalent. This simplified model provides a reference for examining oxygen participation upon further delithiation and the local stabilizing effect of S–O anchoring. Bare and anchored surfaces with the same substrate composition and Li-site occupancies were compared to evaluate the local effect of S–O bonding.

Fig. 1**a** presents the proposed conversion of a BS-derived organosulfonate environment into a surface-bound sulfate-like configuration through S–C bond cleavage and S–O bond formation with surface oxygen. To evaluate the anchoring interaction within a defined model, the adsorption energy of an inorganic sulfur–oxygen model unit consisting of one sulfur atom and three oxygen atoms was calculated on the reference and Li-free surfaces. It changes from −0.57 to −3.96 eV upon removal of all 12 Li atoms (Fig. S1), indicating more favorable adsorption in the computational delithiation limit. The corresponding bare and anchored configurations, denoted B-LNM and LNM@ORC-CEI, respectively, are used to assess the effect of S–O bonding on local oxygen electronic structure and stability.

To investigate the electronic structure changes associated with oxygen redox, the projected density of states (pDOS) of Mn 3*d*, Ni 3*d*, and O 2*p* orbitals was calculated for both B-LNM and LNM@ORC-CEI structures before full delithiation (Fig. 1**b**). In the B-LNM structure, the O 2*p* states dominate near the Fermi level, reflecting the contribution of lattice oxygen to the near-Fermi-level electronic structure [37,38]. In contrast, the LNM@ORC-CEI structure exhibits a distinctly different electronic structure, where the O 2*p* contribution near the Fermi level becomes significantly suppressed for the sulfate-anchored oxygen sites. This result suggests that sulfate anchoring stabilizes these oxygen atoms electronically and reduces their tendency to participate in oxygen redox reactions.

The hole density distributions further reveal the effect of sulfate anchoring on oxygen redox behavior (Fig. 1**c**). In the B-LNM structure before full delithiation, the lattice oxygen located at the surface clearly exhibits hole density, consistent with the involvement of surface lattice oxygen in charge compensation [31,39]. In contrast, the oxygen atoms bonded to sulfate species in the LNM@ORC-CEI structure show negligible hole density at the same Li content. This result indicates local electronic passivation of the anchored oxygen sites within the modeled configuration.

The structural implications of sulfate anchoring were further investigated by analyzing the local geometry around the oxygen sites (Fig. 1**d**). Before full delithiation, the O–O distance near the surface oxygen site in B-LNM is calculated to be 2.57 Å. Upon sulfate anchoring, this distance increases to 2.71 Å with only minor distortion of the

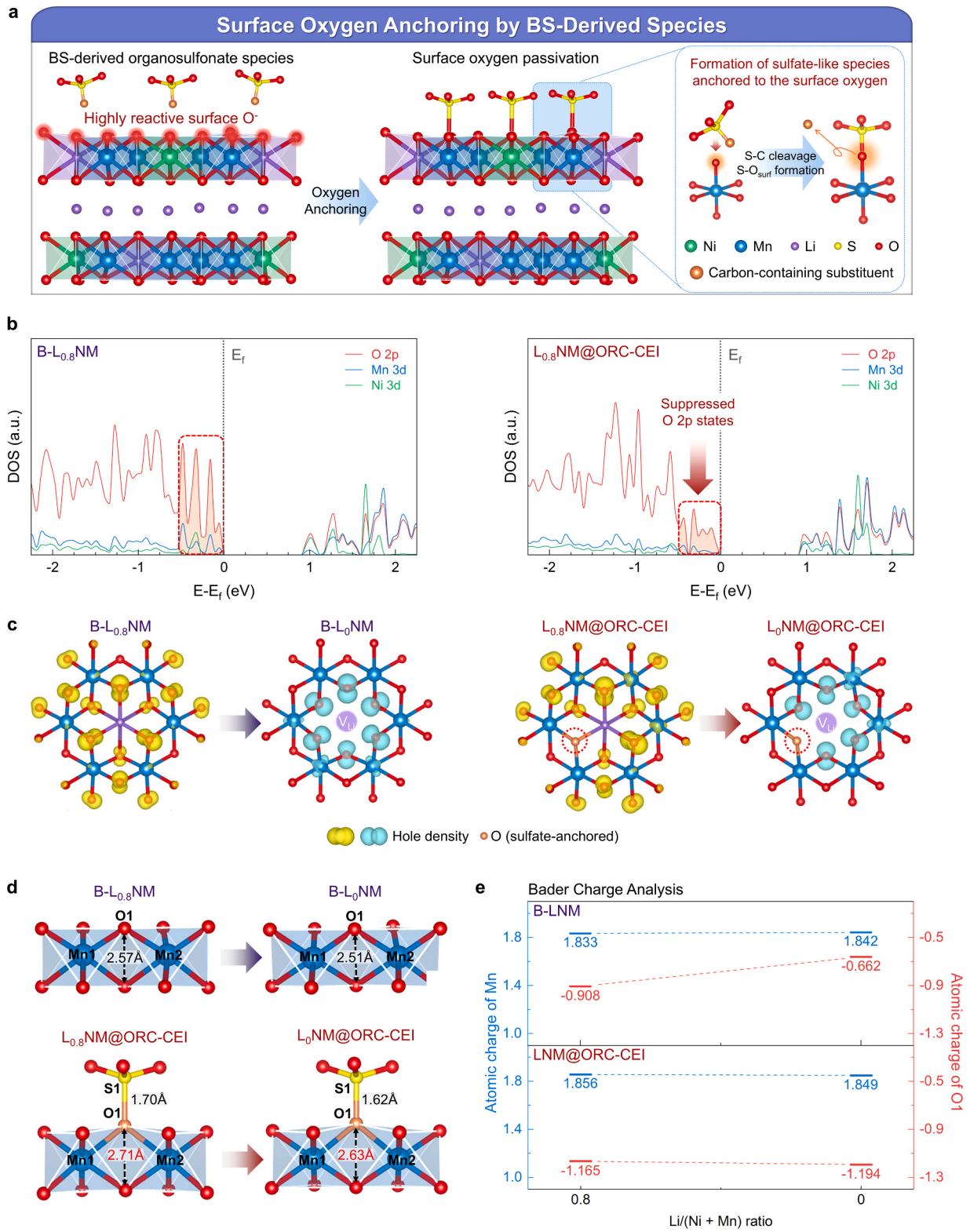


Fig. 1. $L_{0.8}$NM and L_0NM denote the models before (Li/(Ni+Mn) = 0.8) and after full delithiation. (a) Proposed conversion of BS-derived organosulfonate species into surface-oxygen-anchored sulfate-like species through S–C bond cleavage and S–$O_{surface}$ bond formation. Orange spheres denote carbon-containing substituents; the identities of the released carbon-containing products and the detailed proton/electron balance are not established. (b) pDOS of Mn 3*d*, Ni 3*d*, and O 2*p* orbitals for B-LNM and LNM@ORC-CEI before full delithiation. (c) Hole density distributions and (d) structural comparison of the bare and anchored models at the indicated Li contents. (e) Bader charge analysis before and after full delithiation. The substrate before full delithiation is the $Li_{12}Ni_3Mn_{12}O_{36}$ reference model, corresponding to nominal Ni^{4+}/Mn^{4+} states under the formal Li^+ and O^{2-} assignment. The fully delithiated computational limit is obtained by removing all 12 Li atoms. These configurations are used to examine local oxygen participation and the effect of S–O anchoring.

surrounding MnO_6 octahedra. After full delithiation, the sulfate-anchored structure retains an O–O distance of 2.63 Å. The increased O–O separation is consistent with a reduced tendency toward local O–O dimerization [40]. To further quantify the stability of surface lattice oxygen, oxygen-vacancy formation energies were calculated for the bare and SO_3-derived species-anchored LNM surfaces at the same fully delithiated state. For the anchored structure, the surface lattice oxygen directly involved in S–O anchoring was removed, while the corresponding lattice-oxygen site was removed from the bare LNM surface. The oxygen-vacancy formation energy increased from 0.45 eV for bare LNM to 4.60 eV for LNM@ORC-CEI (Fig. S2), corresponding to an increase of 4.15 eV upon S–O anchoring. The higher oxygen-vacancy formation energy indicates that S–O anchoring increases the energetic cost of removing the selected surface lattice oxygen, supporting its stabilization against oxygen loss.

Bader charge analysis further supports the electronic stabilization of lattice oxygen induced by sulfate anchoring (Fig. 1**e**). The effective charges of Mn atoms in both structures remain nearly unchanged before

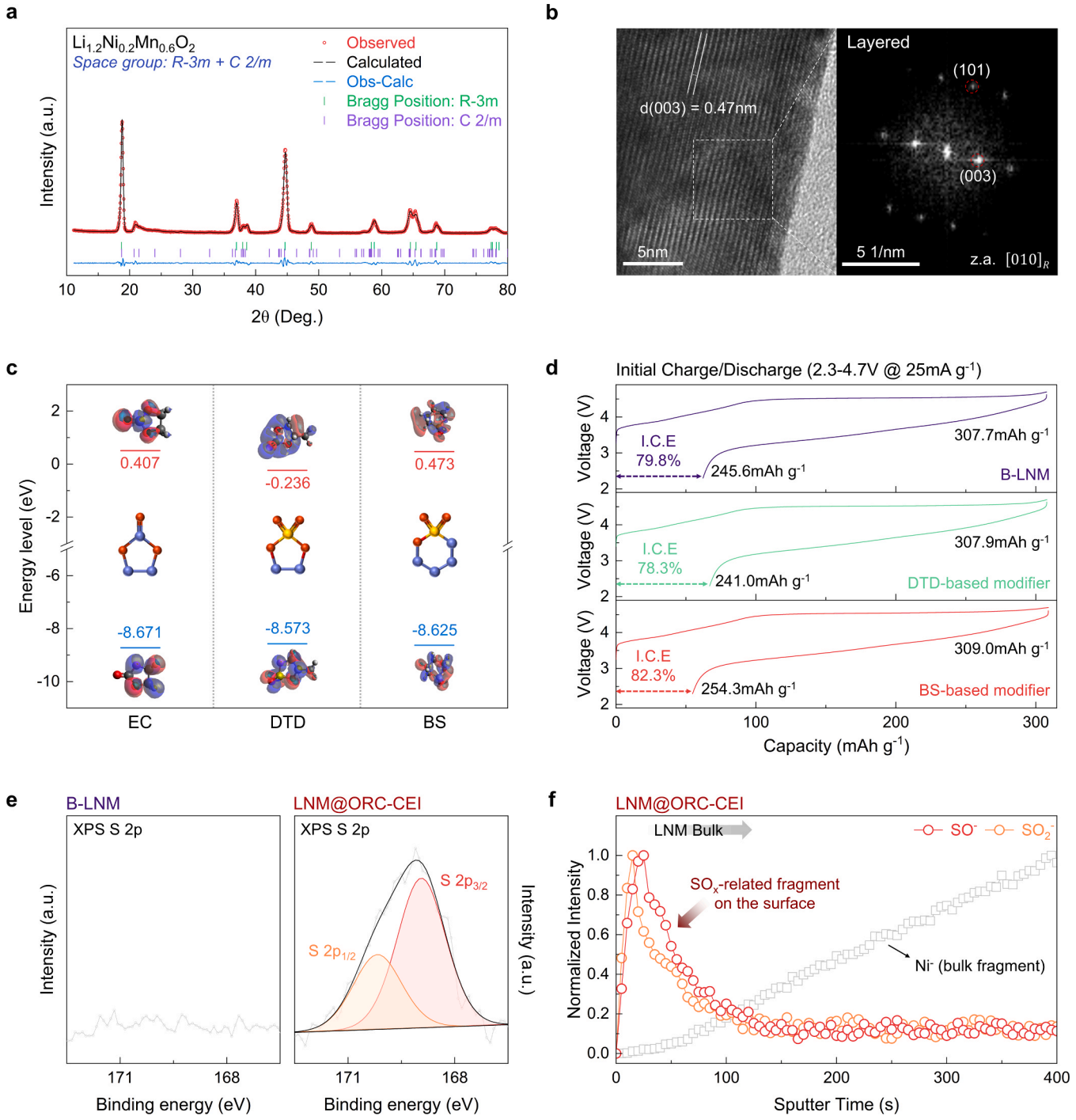


Fig. 2. (a) Rietveld refinement of XRD pattern. (b) HRTEM image with corresponding FFT. The subscript R denotes the zone axis indexed to the R-3m layered structure. (c) HOMO and lowest unoccupied molecular orbital (LUMO) energy levels of EC and the sulfur-containing electrolyte modifiers. (d) Comparison of initial charge/discharge curves in the voltage range of 2.3–4.7 V (*vs.* Li^+/Li) at current density of 25 mA g^{-1}. The first-cycle charge–discharge profiles are representative curves from individual cells. ICE statistics from three independent cells for each condition are reported in the main text. (e) XPS S 2*p* spectra of B-LNM and LNM@ORC-CEI. (f) ToF-SIMS depth profile of LNM@ORC-CEI.

and after full delithiation, indicating limited changes in the local Mn charge during Li extraction. In contrast, lattice oxygen in the B-LNM structure exhibits noticeable charge variation upon full delithiation. However, the sulfate-anchored oxygen in the LNM@ORC-CEI structure maintains a nearly constant effective charge before and after full delithiation, supporting reduced electronic rearrangement at the anchored lattice-oxygen site.

Within the modeled configuration, S–O anchoring reduces hole density at the participating oxygen site, increases the local O–O separation, and raises the energetic cost of removing that lattice oxygen [41]. These results support local electronic passivation of an oxygen site susceptible to irreversible reactions. Such passivation may help preserve electrode-level reversibility by limiting oxygen loss and associated surface degradation, without requiring increased redox activity at the passivated site itself.

2.2. Oxygen-redox-coupled CEI (ORC-CEI) formation in LMR cathodes

To experimentally realize the oxygen-redox-coupled CEI (ORC-CEI) strategy, a Co-free LMR cathode, $Li_{1.2}Ni_{0.2}Mn_{0.6}O_2$ (LNM), was synthesized and employed as the model system. Following the procedure described in the Experimental Section, a transition-metal carbonate precursor was prepared via a co-precipitation route and subsequently lithiated through thermal treatment to obtain the pristine LNM cathode.

The crystallographic structure of LNM was verified by powder X-ray diffraction (XRD) combined with Rietveld refinement (Fig. 2**a**). The diffraction pattern exhibits the characteristic reflections of LMR materials, confirming that the synthesized material consists of a composite layered framework composed of a rhombohedral $Li[TM]O_2$ phase with $R\bar{3}m$ symmetry ($a = b = 2.84996(6)$ Å and $c = 14.2238(4)$ Å) and a monoclinic Li_2MnO_3-like phase with C2/m symmetry ($a = 5.0274(5)$ Å, $b = 8.5636(13)$ Å, and $c = 5.0147(10)$ Å). No detectable impurity reflections were observed. In particular, the superlattice reflections in the 2θ range of 20–32° support the presence of in-plane Li/TM ordering associated with Li_2MnO_3-like domains, which is a representative structural feature of LMR cathodes [42]. Detailed structural information of LNM, including atomic coordinates, occupancy, and isotropic temperature factors (B_{iso}), is summarized in Tables S1 and S2.

The local crystal structure was further examined by high-resolution transmission electron microscopy (HRTEM) (Fig. 2**b**). Clear lattice fringes corresponding to the layered framework were observed, and the measured (003) interplanar spacing of 0.47 nm agrees with $c/3 = 4.74$ Å obtained from the Rietveld-refined lattice parameter $c = 14.2238$ Å. The fast Fourier transform (FFT) pattern further confirms the well-preserved layered structure without detectable structural degradation. In addition, scanning electron microscopy (SEM) and energy-dispersive X-ray spectroscopy (EDS) mapping analyses reveal that LNM consists of spherical secondary particles with an average diameter of approximately 5 μm and that Ni, Mn, and O are homogeneously distributed throughout the particles (Fig. S3).

After confirming the structural integrity of the cathode material, we next investigated how different electrolyte chemistries influence interfacial reactions occurring in the oxygen redox region. In LMR cathodes, the high-voltage region beyond the TM redox limit corresponds to the onset of oxygen redox, where highly reactive lattice oxygen species emerge at the cathode surface. Electrolyte components may form interphases at lower potentials and undergo further reactions in this oxygen redox region.

To systematically examine the influence of interfacial chemistry, two sulfur-containing electrolyte modifiers were selected, namely 1,3,2-dioxathiolane 2,2-dioxide (ethylene sulfate, DTD) [43] and 1,4-butane sultone (BS) [24]. This comparison evaluates the interfacial chemistries derived from these two specific additives, which differ in molecular connectivity, ring structure and decomposition pathways. In density functional theory (DFT) calculations, the highest occupied molecular orbital (HOMO) level reflects oxidative stability; molecules with lower HOMO energies require higher potentials to undergo oxidation. Among the electrolyte modifiers investigated, the sulfur-containing electrolyte modifiers exhibit low HOMO energy, indicating that their oxidative decomposition occurs at a higher potential (Fig. 2**c**). This result suggests relatively high oxidative stability of the sulfur-containing electrolyte modifiers.

The electrochemical influence of these electrolyte systems was first evaluated through galvanostatic charge–discharge measurements between 2.3 and 4.7 V (*vs.* Li^+/Li) at a current density of 25 mA g^{-1} (Fig. 2**d**). The LNM cathode cycled in the base electrolyte without modifiers, denoted as B-LNM, delivered an initial charge capacity of 307.7 mAh g^{-1} with an initial Coulombic efficiency (ICE) of 79.8%.

More notably, the LNM cathode cycled in the DTD-containing electrolyte, denoted as DTD-LNM, exhibited a lower ICE of 78.3% together with a reduced discharge capacity of 241.0 mAh g^{-1} in the representative first-cycle profile. This result indicates that DTD does not improve the initial Coulombic efficiency under the conditions investigated.

In contrast, the electrolyte incorporating BS exhibited a markedly improved electrochemical response. In the representative first-cycle profile, the corresponding LNM cathode, denoted as LNM@ORC-CEI, delivered an initial discharge capacity of 254.3 mAh g^{-1} with an ICE of 82.3%, representing a clear improvement compared with B-LNM as well as DTD-LNM. This improvement suggests that BS-derived interfacial chemistry suppresses irreversible reactions during the initial activation process. The initial Coulombic efficiencies of B-LNM, DTD-LNM, and LNM@ORC-CEI were 79.72 ± 0.09%, 78.29 ± 0.31%, and 82.16 ± 0.24%, respectively, based on three independent cells for each condition (mean ± sample standard deviation).

These results reveal a clear contrast between BS- and DTD-derived interfacial chemistry. While DTD deteriorates both ICE and discharge capacity even compared with B-LNM, BS promotes a significantly improved electrochemical response. Notably, the enhanced performance observed in the BS-containing electrolyte system is proposed to be related to interfacial reactions in the voltage region where oxygen redox is activated. In LMR cathodes, the high-voltage plateau beyond the TM redox limit corresponds to oxygen redox reactions accompanied by the formation of highly reactive lattice oxygen species at the cathode surface.

Here, oxygen-redox coupling refers to the proposed connection between activation of reactive surface oxygen and further transformation of pre-existing SO_3-containing interphase species during high-voltage charging. In the proposed model, S–O bonding with surface oxygen produces a surface-bound sulfate-like environment that locally passivates the participating oxygen.

To confirm the incorporation of BS into the electrolyte, ^{13}C NMR spectroscopy was conducted for the BS-containing electrolyte formulation (Fig. S4). The characteristic signals of BS were clearly observed without noticeable additional resonances, verifying the chemical integrity of BS in the electrolyte prior to electrochemical evaluation.

The formation of sulfur-derived interphase species during the initial cycle was further examined by X-ray photoelectron spectroscopy (XPS) and time-of-flight secondary ion mass spectrometry (ToF-SIMS) analyses. After the first charge, the XPS spectra of the LNM electrode cycled in the BS-containing electrolyte system exhibit clear signatures of S–O bonding configurations, indicating the formation of sulfur-derived surface species (Fig. 2**e**) [44]. Consistently, ToF-SIMS analyses reveal the presence of SO_x-related fragments on the surface of the cycled electrode, with depth profiles showing that these sulfur-containing species are concentrated near the cathode surface (Fig. 2**f**) [45]. These results identify S–O-based interphase species on the LNM surface during the initial activation process, consistent with the proposed ORC-CEI model.

To examine the voltage dependence of BS-derived interphase chemistry, S 2*p* XPS spectra were collected from LNM electrodes charged to 4.3, 4.5, and 4.7 V (Fig. S5). The S 2*p* signal is weak at 4.3 V. At 4.5 V, the spectrum is dominated by the contribution assigned to

organosulfonate-like species, whereas the sulfate-like contribution increases at 4.7 V. Complementary ToF-SIMS spectra show decreased $C_4H_7SO_3^-$ and $C_4H_9SO_3^-$ signals and increased SO_4^- and HSO_4^- signals between 4.5 and 4.7 V (Fig. S6). These observations support further transformation of the pre-existing sulfur-containing interphase toward sulfate-like environments during charging through the high-voltage oxygen-redox region.

BS-derived organosulfonate species are considered possible precursors to the proposed surface-anchored interphase. Here, "SO_3-containing moiety" denotes the sulfur–oxygen unit within such an organic species. Signals assigned to $C_4H_7SO_3^-$ and $C_4H_9SO_3^-$ at 4.5 V support the presence of BS-related organic sulfur species (Fig. S6). Ring opening followed by subsequent reactions provides a possible route to these species [24].

The subsequent decrease in organosulfonate-related fragments and increase in sulfate-related fragments motivate a proposed interfacial bond-reorganization model involving S–C bond cleavage and S–O bond formation with reactive cathode surface oxygen (Fig. 1**a**). Within this model, the participating oxygen remains connected to the cathode framework, and the resulting surface-bound sulfate-like environment locally passivates that oxygen.

DTD was evaluated at the same additive mass fraction as BS (1.5 wt %) in the same baseline electrolyte. At 4.7 V, the DTD-containing LNM electrode exhibits sulfate-related S 2*p* XPS signatures and SO_4^-/HSO_4^- fragments in ToF-SIMS (Figs. S7 and S8). The observation of sulfate-like products in both systems, together with their different electrochemical performance, indicates that the presence of such products alone is insufficient to explain the stabilization observed with BS. This comparison motivates consideration of the formation pathways and surface interactions of the sulfur-containing species, including the proposed S–O linkage between an SO_3-containing precursor and reactive surface oxygen.

The BS-containing LNM electrode exhibits stronger $MnSO_4^-$ and $NiSO_4^-$ signals at 4.7 V than at 4.5 V and than the DTD-containing LNM electrode charged to 4.7 V (Figs. S6 and S8). These fragments are consistent with an association between sulfur–oxygen species and transition-metal-containing surface regions.

For comparison, a $LiFePO_4$ (LFP) electrode was charged to 4.7 V and held at this potential for 5 h in the same BS-containing electrolyte. Relative to LNM charged to 4.7 V, LFP exhibits stronger C_4 sulfonate-related fragment signals and weaker SO_4^- and HSO_4^- signals, while its S 2*p* spectrum is dominated by the organosulfonate-like contribution (Figs. S7 and S8). Prolonged exposure to the same upper potential on LFP therefore does not reproduce the interphase signature observed on LNM. This comparison supports a role for cathode surface chemistry in the transformation.

2.3. *Electrochemical stabilization of LMR cathodes enabled by ORC-CEI formation*

The electrochemical performance of LNM was evaluated after an initial formation cycle between 2.3 and 4.7 V at 25 mA g^{-1}. Subsequent cycling between 2.3 and 4.5 V at 125 mA g^{-1} was used to examine the persistence of the stabilization following high-voltage activation (Fig. 3**a**). B-LNM exhibited gradual capacity decay, retaining only 57% of its initial capacity after 100 cycles. Notably, DTD-LNM provided only limited improvement, retaining 61% of its initial capacity after 100 cycles. In contrast, LNM@ORC-CEI demonstrated significantly improved cycling stability, maintaining 79% of its initial capacity after 100 cycles, representing a clear improvement compared with all other CEI chemistries investigated. Additional BS-content-dependent cycling retention data are provided in Fig. S9. This result highlights the critical role of BS-derived interfacial chemistry in stabilizing the electrochemical reaction of LNM under high-voltage operation.

To evaluate cycling stability under the voltage conditions used for the mechanistic investigations, additional half-cell tests were performed between 2.3 and 4.7 V at 125 mA g^{-1} following an initial formation cycle at 25 mA g^{-1} (Fig. S10). After 70 cycles, LNM@ORC-CEI exhibited a capacity retention of 67%, compared with 44% for DTD-LNM and 37% for B-LNM. These results demonstrate that the improved capacity retention with the BS-containing electrolyte persists under repeated cycling at an upper cutoff voltage of 4.7 V.

To further evaluate the stability of the electrochemical reaction beyond capacity retention, the evolution of the average discharge voltage during cycling was quantitatively analyzed (Fig. 3**b**). B-LNM exhibited a substantial voltage decay of approximately 0.32 V over 100 cycles, indicating severe structural degradation and accumulated polarization. Similarly, DTD-derived CEI chemistry showed pronounced voltage fading with a voltage drop of 0.31 V over 100 cycles, consistent with its poor cycling stability. On the other hand, LNM@ORC-CEI exhibited significantly suppressed voltage decay, with a minimal voltage drop of only 0.13 V after 100 cycles. This markedly reduced voltage fading supports the contribution of interfacial stabilization to improved electrochemical reversibility under high-voltage operation.

The voltage decay behavior was further examined using normalized voltage profiles. In B-LNM, the discharge curves progressively shift toward lower voltages during cycling, reflecting significant voltage decay associated with structural degradation of the layered framework (Fig. 3**c**). In contrast, LNM@ORC-CEI exhibits substantially suppressed voltage shifts and maintains a more stable discharge voltage even after prolonged cycling (Fig. 3**d**).

Further insight into the redox behavior was obtained from differential capacity (dQ/dV) analysis (Fig. S11). In B-LNM, the redox peaks progressively shift and broaden as cycling proceeds, indicating increased polarization and gradual degradation of the electrochemical reactions. By contrast, LNM@ORC-CEI maintains sharper and more stable redox peaks throughout cycling, suggesting improved reversibility of the redox processes and reduced electrochemical polarization.

The improved interfacial stability also leads to enhanced rate capability (Fig. 3**e–f**). At a low current density of 0.1 C, LNM@ORC-CEI delivers a discharge capacity of 219.7 mAh g^{-1}, higher than the 215.6 mAh g^{-1} of B-LNM. However, as the current density increases, the performance gap widens considerably. At 3 C, LNM@ORC-CEI retains 131.6 mAh g^{-1} compared with only 71.1 mAh g^{-1} for B-LNM, demonstrating that the ORC-CEI effectively reduces interfacial resistance and supports more facile Li^+ transport kinetics under high-rate conditions [46]. In the rate-capability test with 5 cycles at each current density (Fig. S12), LNM@ORC-CEI recovers 88.7% of its initial capacity, indicating better stability than B-LNM.

Electrochemical impedance spectroscopy (EIS) was used to compare interfacial resistance after the 1st and 100th cycles (Fig. 3**g–h**). The fitted charge-transfer resistance (R_{ct}) of B-LNM increases from 21.6 ± 1.9 to 101.6 ± 6.9 Ω, whereas that of LNM@ORC-CEI increases from 14.4 ± 1.4 to 43.0 ± 13.2 Ω (Table S3). The uncertainties are the parameter uncertainties reported by ZMAN, which are derived from the covariance matrix of the modulus-weighted complex nonlinear least-squares fit and do not represent cell-to-cell variation. These results indicate a smaller increase in the fitted charge-transfer resistance for LNM@ORC-CEI during cycling, consistent with mitigated interfacial degradation [47].

The practical relevance of the ORC-CEI strategy was evaluated through full-cell cycling tests between 2.25 and 4.45 V (Fig. 3**i**). Full cells were assembled using an LNM cathode paired with a graphite anode under a sufficiently balanced N/P ratio of 1.3. Under these conditions, the full cell employing LNM@ORC-CEI exhibited significantly improved cycling stability compared with the B-LNM full cell. After 200 cycles, the LNM@ORC-CEI full cell retained 81% of its initial capacity, whereas the B-LNM full cell retained only 68%. These results demonstrate that ORC-CEI formation not only improves half-cell electrochemical stability but also effectively stabilizes LNM cathodes under practical full-cell operating conditions.

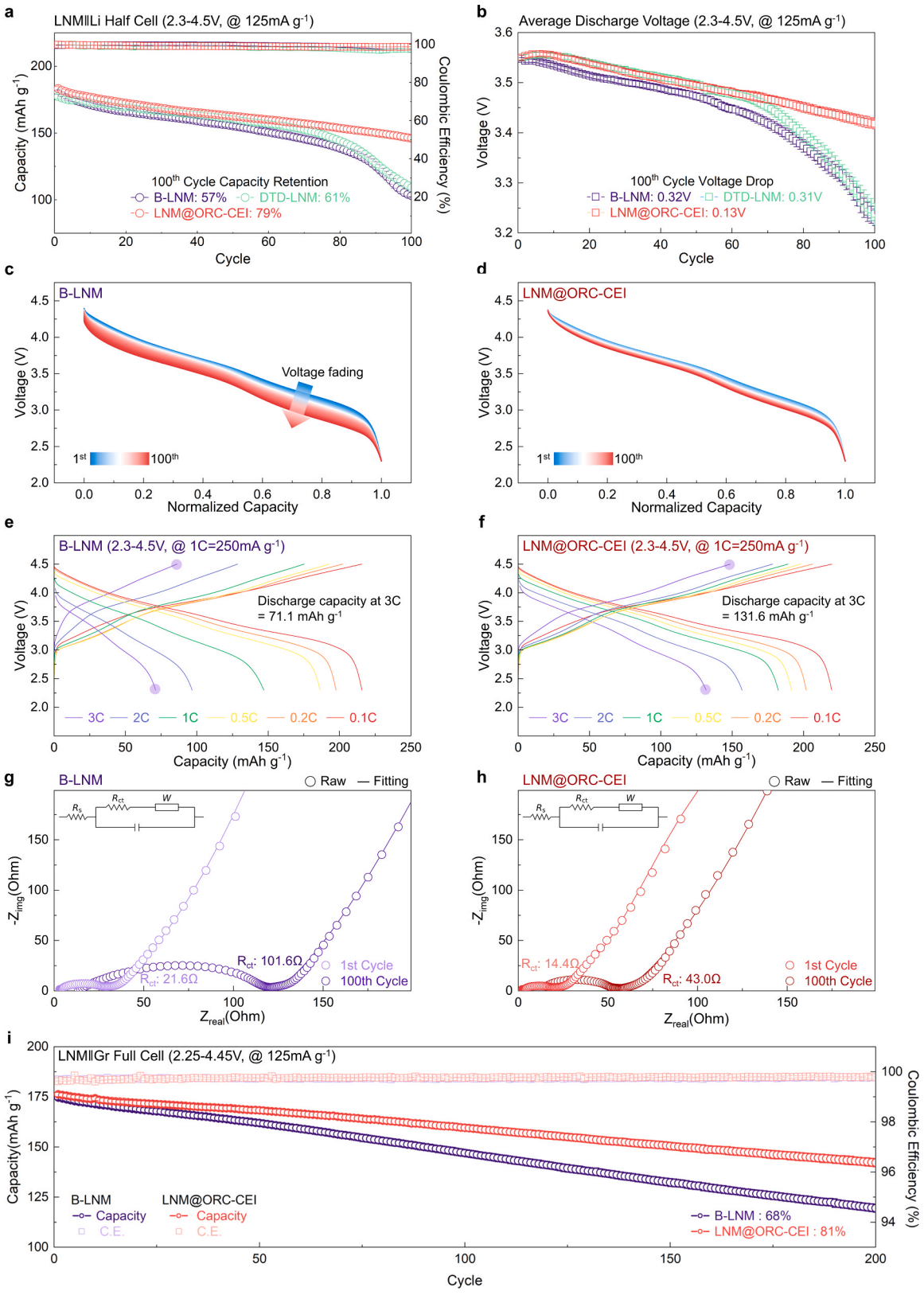


Fig. 3. Comparison of (a) discharge capacity and (b) average discharge voltage over 100 cycles between 2.3 and 4.5 V at 125 mA g^{-1}. Normalized discharge profiles over 100 cycles for (c) B-LNM and (d) LNM@ORC-CEI. Charge/discharge profiles of (e) B-LNM, (f) LNM@ORC-CEI at various current densities. EIS results for (g) B-LNM and (h) LNM@ORC-CEI after the 1st and 100th cycles. (i) Discharge capacity over 200 cycles in graphite full cell between 2.25 and 4.45 V. For the half-cell cycling results in (a–d), an initial formation cycle between 2.3 and 4.7 V at 25 mA g^{-1} preceded cycling between 2.3 and 4.5 V at 125 mA g^{-1}. The formation cycle is excluded from the cycle count in the cycling-performance plots. Discharge capacities in (a) and (i) and average discharge voltages in (b) are presented as mean ± standard deviation from three independent cells for each condition.

2.4. Stabilization of surface oxygen and structural evolution by ORC-CEI formation

To elucidate the mechanistic origin of the improved electrochemical stability enabled by ORC-CEI formation, a combination of *operando* XRD, in-situ differential electrochemical mass spectrometry (DEMS), synchrotron-based X-ray absorption spectroscopy (XAS), and post-cycling HRTEM analyses was performed.

Operando XRD measurements were first performed to monitor the structural evolution of LNM during the initial charge/discharge cycle. In

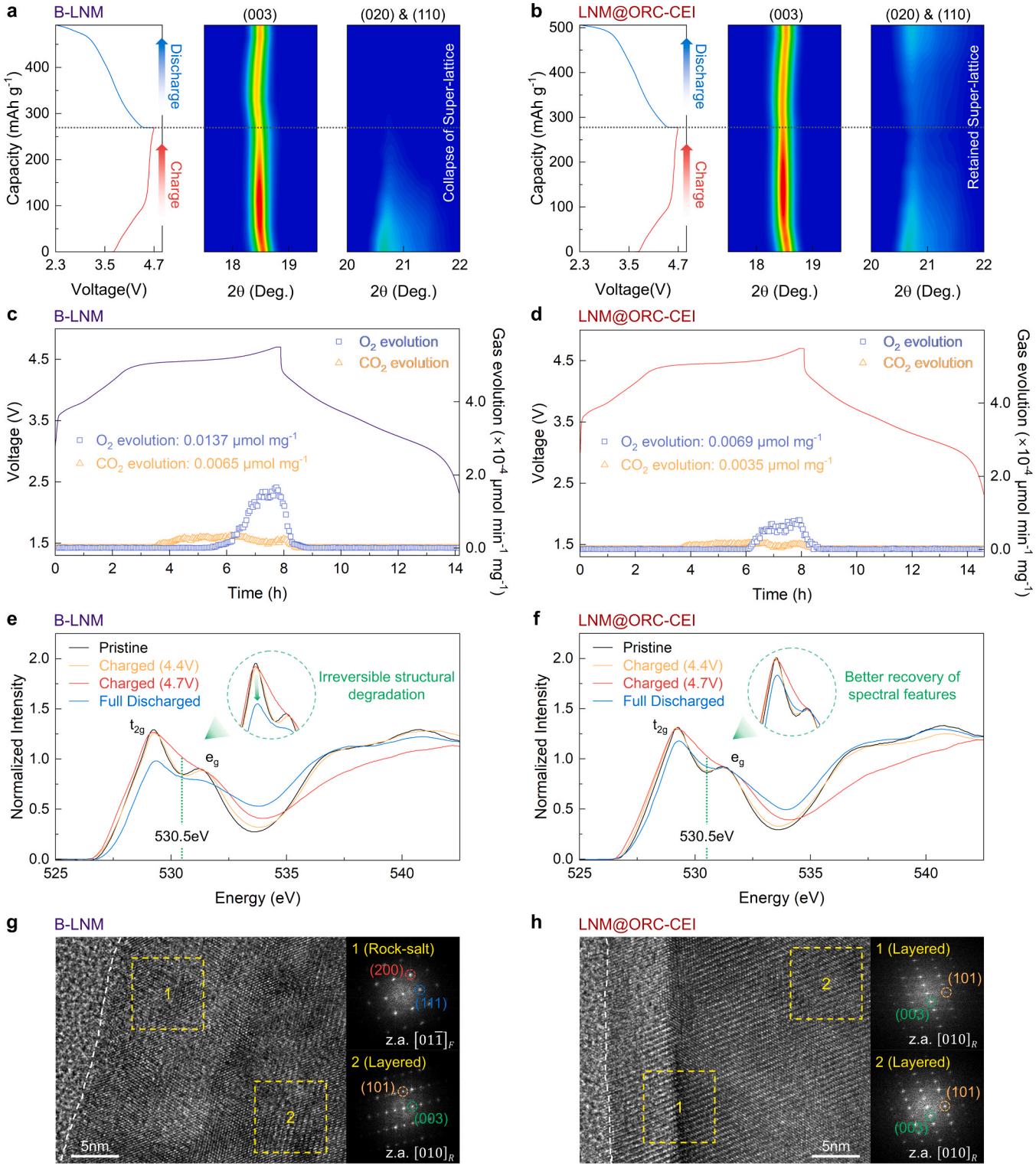


Fig. 4. *Operando* XRD 2D contour map of (a) B-LNM and (b) LNM@ORC-CEI during first cycle. (c,d) Calibrated O_2 and CO_2 evolution rates (μmol min^{-1} mg^{-1}) normalized to the cathode active mass during the first cycle between 2.3 and 4.7 V at 30 mA g^{-1} for (c) B-LNM and (d) LNM@ORC-CEI. Integration over the entire first charge–discharge cycle yields cumulative O_2/CO_2 evolution of 0.0137/0.0065 μmol mg^{-1} for B-LNM and 0.0069/0.0035 μmol mg^{-1} for LNM@ORC-CEI. O K-edge sXAS spectra of (e) B-LNM and (f) LNM@ORC-CEI. HRTEM image with corresponding FFT in (g) B-LNM and (h) LNM@ORC-CEI. Subscripts R and F denote zone axes indexed to the R-3m layered and Fm-3m rock-salt structures, respectively.

LMR cathodes, the most critical structural signature during the activation process is the stability of the superlattice reflections associated with Li_2MnO_3-like ordering, which provide an indirect indicator of local structural ordering.

In B-LNM (Fig. 4**a**), the superlattice reflections gradually weaken during the first charge and nearly disappear at the end of the charging process. This behavior is consistent with a loss of Li_2MnO_3-like ordering during oxygen-redox activation. In contrast, LNM@ORC-CEI (Fig. 4**b**) retains clearly identifiable superlattice reflections even near the end of the charging process, consistent with better preservation of local Li_2MnO_3-like ordering during the initial oxygen-redox activation.

Another notable difference is observed in the evolution of the (003) reflection. In B-LNM, the disappearance of the superlattice reflections is accompanied by a noticeable reduction in the (003) peak intensity near the end of charging, indicating progressive structural disorder within the layered framework. By contrast, LNM@ORC-CEI maintains a relatively stable (003) peak intensity throughout the initial cycle, suggesting improved structural integrity of the layered lattice. For clarity, these results highlight selected diffraction regions that capture the key structural evolution during the initial activation process, while the full *operando* XRD patterns of B-LNM and LNM@ORC-CEI are provided in Figs. S13 and S14.

To further probe the evolution of lattice oxygen during the activation process, in-situ DEMS measurements were conducted during the first charge–discharge cycle. In B-LNM (Fig. 4**c**), pronounced O_2 and CO_2 evolution signals are detected during the high-voltage plateau region corresponding to oxygen-redox activation. The evolution of these gases is associated with oxygen release and parasitic electrolyte oxidation reactions occurring at high states of charge [48].

LNM@ORC-CEI (Fig. 4**d**) exhibits markedly suppressed O_2 and CO_2 evolution throughout the high-voltage region. Integration over the entire first charge–discharge cycle shows that cumulative O_2 evolution decreased from 0.0137 μmol mg^{-1} for B-LNM to 0.0069 μmol mg^{-1} for LNM@ORC-CEI, while the corresponding CO_2 evolution decreased from 0.0065 to 0.0035 μmol mg^{-1} (Fig. 4**c,d**). These measurements establish reduced gas-phase O_2 evolution under the measurement conditions, consistent with suppression of irreversible oxygen-release reactions.

To examine the TM–O electronic structure, O K-edge soft X-ray absorption spectroscopy (sXAS) was performed (Fig. 4**e–f**). The pre-edge region corresponds to the hybridized TM 3*d*–O 2*p* states, including the feature near 530–531 eV [49]. Upon charging to the high-voltage region, both B-LNM and LNM@ORC-CEI exhibit an increased intensity of this feature, indicating changes in the TM–O electronic structure in both electrodes.

During discharge, the O K-edge spectral features of LNM@ORC-CEI recover more closely toward the initial spectrum than those of B-LNM (Fig. 4**e–f**). This observation is consistent with more reversible evolution of the hybridized TM–O electronic structure. Because the pre-edge features are affected by TM–O hybridization, their recovery is not treated as an independent measurement of reversible oxygen-redox capacity.

Additional insight into transition-metal redox behavior was obtained from Ni and Mn K-edge X-ray absorption near-edge structure (XANES) analyses. Both B-LNM and LNM@ORC-CEI exhibit similar spectral shifts at the Ni K-edge during charge and discharge, confirming that the Ni^{2+}/Ni^{4+} redox process proceeds comparably in both systems (Fig. S15). In contrast, the Mn K-edge spectra reveal a clear difference during discharge. While Mn remains predominantly in the Mn^{4+} state in LNM@ORC-CEI, B-LNM exhibits a more pronounced reduction of Mn^{4+} upon discharge, which may be associated with irreversible TM migration into the Li layer and the associated conversion of the layered framework toward spinel- or rock-salt-like phases during the oxygen-redox process (Fig. S16).

Further analysis of the local coordination environment using Mn K-edge extended X-ray absorption fine structure (EXAFS; Fig. S17) indicates that the Mn–O coordination-shell feature in LNM@ORC-CEI evolves more reversibly during charge and discharge, returning close to its initial position after discharge. In contrast, B-LNM exhibits a noticeable deviation of the Mn–O bonding environment after the cycle, suggesting irreversible distortion of the Mn–O framework. These qualitative comparisons suggest that ORC-CEI formation helps preserve the local Mn–O bonding environment during the oxygen-redox process.

The suppression of oxygen release during the initial activation process is expected to significantly influence the long-term structural stability of LNM. To examine the resulting structural integrity after prolonged cycling, post-cycling HRTEM images and their corresponding FFT patterns were analyzed. After extended cycling, B-LNM exhibits severe surface reconstruction characterized by the formation of rock-salt-like domains and local structural collapse (Fig. 4**g**). In contrast, LNM@ORC-CEI retains a well-preserved layered structure with minimal surface reconstruction, suggesting that ORC-CEI protects the cathode surface from structural degradation during repeated electrochemical operation (Fig. 4**h**). Further HRTEM analysis supports the interfacial stabilization effect of ORC-CEI (Fig. S18). B-LNM exhibits a heterogeneous CEI layer, indicating nonuniform interphase growth during cycling. In contrast, LNM@ORC-CEI maintains a uniform CEI layer with a thickness of 1.3 nm. This more uniform interphase suggests that ORC-CEI effectively suppresses nonuniform interphase growth during cycling.

These results collectively support the proposed mechanism in which surface-oxygen passivation suppresses oxygen release and associated surface reconstruction, helping preserve the structural integrity and reversible electrochemical response of LNM during cycling.

2.5. Suppression of structural and interfacial degradation during long-term cycling of LMR cathodes via ORC-CEI formation

To evaluate the structural stability of the cathode under prolonged full-cell operation, the cycled LNM electrodes were examined by ex-situ XRD after 200 cycles (Fig. 5**a**). The intensity ratio between the (003) and (104) reflections, I(003)/I(104), is commonly used as an indicator of cation mixing in layered oxide cathodes [50]. The pristine LNM exhibits an I(003)/I(104) ratio of 2.18, indicating a well-ordered layered structure. After 200 cycles, LNM@ORC-CEI retains a relatively high I(003)/I(104) value of 2.01, whereas the ratio in B-LNM decreases to 1.83. The more pronounced reduction in B-LNM is consistent with greater loss of structural ordering during cycling. In contrast, the higher I(003)/I(104) ratio maintained in LNM@ORC-CEI is consistent with better preservation of the layered framework.

The morphological evolution of cathode particles after 200 cycles was further investigated through the ex-situ SEM analysis. The cycled B-LNM cathode exhibits extensive microcrack formation and fragmentation of the secondary particles (Fig. 5**b**). These cracks are typically induced by the mechanical strain accumulated during repeated delithiation and lithiation processes. Once formed, such microcracks can serve as pathways for electrolyte penetration into the interior of secondary particles, accelerating internal degradation reactions and facilitating the accumulation of resistive interfacial species along primary-particle boundaries.

In contrast, the LNM@ORC-CEI cathode retains a largely intact secondary-particle morphology with smooth particle surfaces and significantly reduced crack formation (Fig. 5**c**). The improved morphological stability suggests that the ORC-CEI effectively stabilizes the cathode–electrolyte interface, thereby mitigating surface-initiated degradation and suppressing the propagation of microcracks during prolonged cycling.

The influence of cathode stabilization on the anode side was also examined by analyzing the graphite electrode morphology after cycling (Fig. S19). The graphite anode paired with B-LNM exhibits noticeable surface deterioration and film-like surface deposits, indicating significant parasitic reactions induced by cathode-derived species. In contrast, the graphite anode cycled with LNM@ORC-CEI maintains a cleaner and more uniform surface morphology, suggesting that ORC-CEI formation

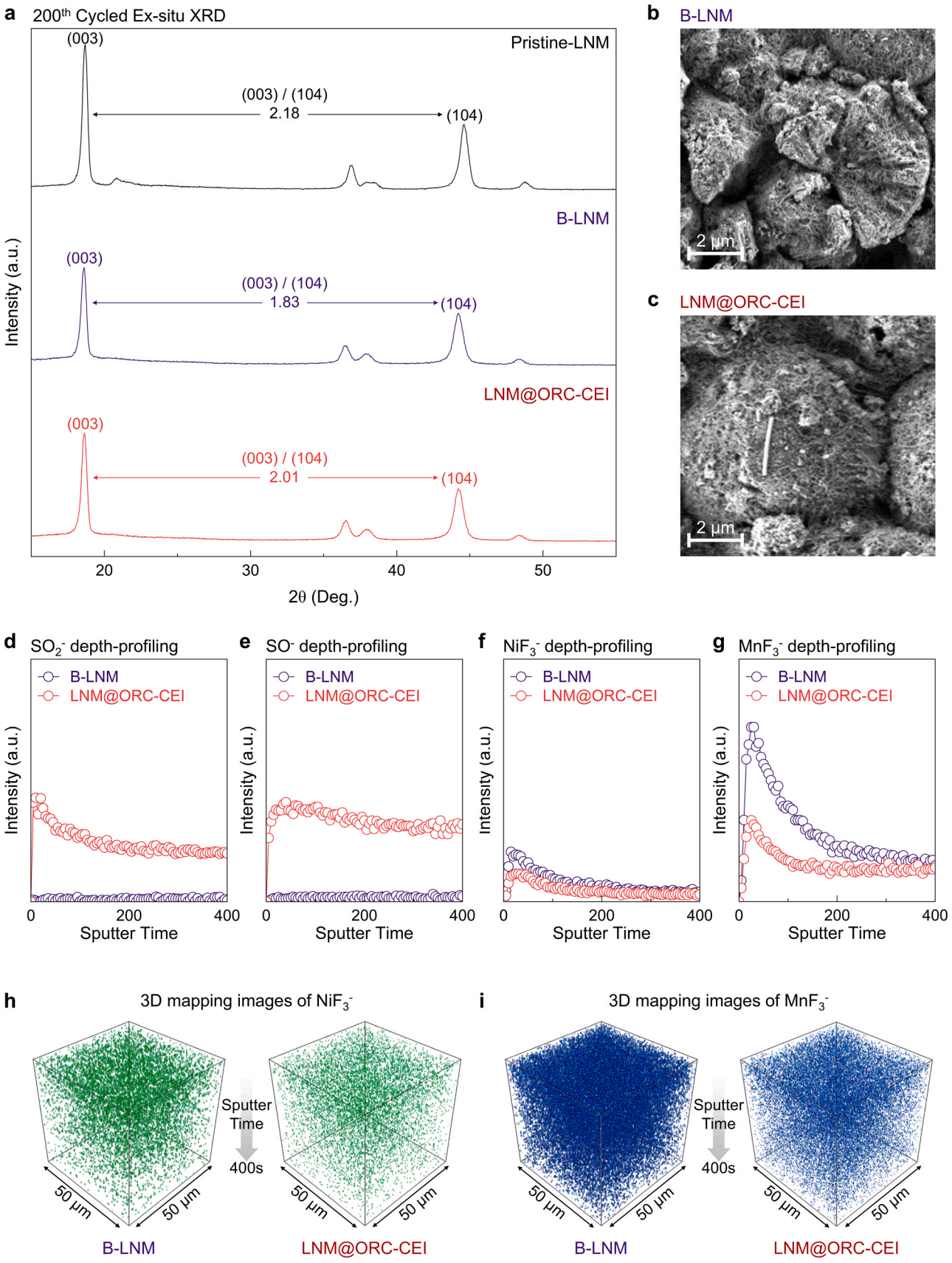


Fig. 5. (a) 200th cycled ex-situ XRD patterns of B-LNM and LNM@ORC-CEI. SEM images of cathode in cycled (b) B-LNM||graphite full cell and (c) LNM@ORC-CEI||graphite full cell. ToF-SIMS depth profile comparing B-LNM and LNM@ORC-CEI for (d) SO_2^-, (e) SO^-, (f) NiF_3^-, (g) MnF_3^- fragments. ToF-SIMS 3D mapping images of (h) NiF_3^- and (i) MnF_3^- for B-LNM and LNM@ORC-CEI.

suppresses detrimental cathode–anode cross-talk during cycling. SEM-EDS analysis (Figs. S20 and S21) indicates that these deposits are associated with cathode-derived byproducts, which is consistent with transition-metal dissolution and the migration of CEI/SEI cross-talk species from the cathode to the anode during cycling.

ToF-SIMS depth profiling and 3D mapping were used to examine interphase chemistry after prolonged cycling. SO_2^- and SO^- signals remain enriched in LNM@ORC-CEI, supporting persistent retention of sulfur-derived interphase components (Fig. 5**d–e**). The lower NiF_3^- and MnF_3^- signals and their weaker spatial distributions indicate reduced accumulation of TM–F-containing species at the cathode surface compared with B-LNM (Fig. 5**f–i**). Such fragments have been associated with reactions involving transition-metal species and electrolyte-derived fluorides [51]. These observations are consistent with mitigated interfacial degradation and reduced accumulation of potentially resistive products during cycling.

3. Conclusion

This work investigates an oxygen-redox-coupled interphase strategy based on the proposed chemical functionality of SO_3-containing moieties toward reactive surface oxygen in LMR cathodes, using BS as a molecular precursor. Voltage-resolved XPS and ToF-SIMS support further transformation of BS-derived organosulfonate-related species toward sulfate-like environments during high-voltage charging. In the proposed bonding model, S–O linkage formation connects the sulfur-containing moiety to cathode surface oxygen and produces a surface-bound sulfate-like configuration. Calculations using a nominal Ni^{4+}/Mn^{4+} reference model show reduced hole density at the anchored oxygen and a higher energetic cost of its removal, supporting local electronic passivation within the modeled environment.

Calibrated DEMS shows reduced gas-phase O_2 evolution, while diffraction, XAS, and post-cycling microscopy indicate better preservation of structural ordering, TM–O environments, and surface structure. ToF-SIMS further supports persistent sulfur-containing interphase components and reduced accumulation of TM–F-containing species. Together, these observations support suppression of irreversible surface degradation and improved electrochemical reversibility.

Following an initial formation cycle to 4.7 V, LNM@ORC-CEI retains 79% of its capacity after 100 cycles over 2.3–4.5 V at 125 mA g^{-1}, compared with 57% for B-LNM, and reduces voltage decay from 3.2 to 1.3 mV per cycle. Its capacity at 3 C is 131.6 mAh g^{-1}, compared with 71.1 mAh g^{-1} for B-LNM. During repeated cycling over 2.3–4.7 V, capacity retention after 70 cycles is 67%, compared with 44% for DTD-LNM and 37% for B-LNM. Graphite full cells retain 81% of their capacity after 200 cycles over 2.25–4.45 V, compared with 68% for the baseline system. These results motivate interphase design that considers the chemical interaction with reactive surface oxygen alongside the protective properties of the resulting film.

4. Experimental

4.1. Preparation of electrolyte and electrode

B-LNM's electrolyte consisted of 1.2 M $LiPF_6$ dissolved in ethylene carbonate (EC)/ethyl methyl carbonate (EMC)/dimethyl carbonate (DMC) (2:4:4 vol%). LNM@ORC-CEI's electrolyte (1.2 M $LiPF_6$ dissolved in EC/EMC/DMC (2:4:4 vol%) + 1.5 wt% 1,4-butane sultone) was prepared in an Ar-filled glove box. For comparison, a DTD-containing electrolyte was prepared by adding 1.5 wt% ethylene sulfate to the baseline electrolyte of 1.2 M $LiPF_6$ in EC/EMC/DMC (2:4:4 vol%). The $Ni_{0.25}Mn_{0.75}CO_3$ precursor was prepared by co-precipitation under N_2 using a 2 M mixed $NiSO_4$/$MnSO_4$ solution (Ni:Mn = 25:75), supplied at 0.22 L h^{-1}, together with 2 M Na_2CO_3 and 0.2 M aqueous NH_3 solutions. The reaction was maintained at 55 °C and pH 8.00 for 3 h, followed by aging for 3 h under the same conditions. The precursor was washed with deionized water until the filtrate was neutral and dried at 100 °C for 24 h. The precursor was mixed with Li_2CO_3 using hand-milling at a Li:TM molar ratio of 1.5. The LNM mixture was calcined at 900 °C for 10 h under air flow. The LNM cathodes were fabricated by applying a slurry composed of 92 wt% LNM as the active material, 4 wt% conductive carbon, and 4 wt% polyvinylidene fluoride. N-Methyl-2-pyrrolidinone (NMP) was used as the solvent, and the slurry was cast on a carbon-coated Al current collector using a doctor blade. The cathode was then dried in a vacuum oven at 100 °C overnight. The active mass loading of the cathode was 12 mg cm^{-2}. The graphite anode was fabricated by applying a slurry composed of 92 wt% graphite as the active material, 2 wt% conductive carbon, 3 wt% carboxymethyl cellulose, and 3 wt% styrene butadiene rubber. Deionized water was used as the solvent, and the slurry was cast on a Cu current collector using a doctor blade. The anode was then dried in a vacuum oven at 100 °C for 2 h. The active mass loading of the anode was 8.5 mg cm^{-2}.

4.2. Electrochemical characterization

Electrochemical performance was evaluated using CR2032-type coin cells assembled in an Ar-filled glove box. For half-cell tests, cells contained a polypropylene separator (Celgard 2400). For full-cell tests, cells contained a glass fiber separator (GF/F). Each coin cell contained 0.1 mL of electrolyte, corresponding to approximately 53 mL Ah^{-1} based on the nominal cathode capacity. The cathode and graphite anode active mass loadings were 12 and 8.5 mg cm^{-2}, corresponding to areal capacities of 2.40 and 3.06 mAh cm^{-2} at specific capacities of 200 and 360 mAh g^{-1}, respectively. The cathode and anode diameters were 10 and 14 mm. The N/P ratio was approximately 1.3, calculated from the anode-to-cathode areal-capacity ratio on an equal-area basis. Galvanostatic charge/discharge tests were carried out using a battery charge/discharge system (WBCS 3000, WonATech). For the cycling tests with an upper cutoff voltage of 4.5 V, half-cells underwent an initial formation cycle between 2.3 and 4.7 V at 25 mA g^{-1}, followed by long-term cycling between 2.3 and 4.5 V at 125 mA g^{-1}. For the additional high-voltage half-cell tests, cells underwent the same formation cycle, followed by cycling between 2.3 and 4.7 V at 125 mA g^{-1} using the baseline, BS-containing, and DTD-containing electrolytes. Full cells were tested between 2.25 and 4.45 V, with an initial formation cycle at 25 mA g^{-1} followed by cycling at 125 mA g^{-1}. All current densities were calculated based on the cathode active-material mass. For both half-cells and full cells, the formation cycle was excluded from the cycle count in the cycling-performance plots. For the additional 2.3–4.7 V half-cell tests, capacity retention was calculated relative to the discharge capacity of the first cycle at 125 mA g^{-1} after formation. The key electrochemical comparisons were performed using three independent cells for each condition. ICE was calculated individually for each cell as the first-cycle discharge capacity divided by the corresponding charge capacity, multiplied by 100%, and is reported as mean ± sample standard deviation. For the cycling comparisons, discharge capacities and average discharge voltages were averaged across the independent cells at each cycle, and error bars represent the sample standard deviation. Electrochemical impedance spectroscopy (EIS) was performed using a ZIVE MP2F system (WonATech). Before EIS measurements, cells were discharged to 2.3 V and rested at open circuit for 24 h at 25 °C. Nyquist spectra were collected over a frequency range from 1 MHz to 10 mHz with an amplitude of 10 mV and fitted using ZMAN software with a Randles-type equivalent circuit (Fig. 3**g**), in which the ohmic resistance (R_s) is connected in series with a constant phase element (CPE) in parallel with the charge-transfer resistance (R_{ct}) and a finite-length Warburg element (W). Because the interphase and charge-transfer contributions were not resolved as separate semicircles, they are represented by a single R_{ct}. The measurement cycle numbers are specified in the figure captions. Fitted resistances are reported in Table S3 as the best-fit parameter ± the parameter uncertainty reported by ZMAN, which is derived from the

covariance matrix of the modulus-weighted complex nonlinear least-squares fit. These uncertainties arise from equivalent-circuit fitting and do not represent cell-to-cell variation.

4.3. Materials characterization

Cells were disassembled in an Ar-filled glove box. For the surface analyses, washed electrodes were rinsed three times with dimethyl carbonate for 1 min each and twice with acetonitrile for 10 min each. All recovered electrodes were dried under vacuum at room temperature for 8 h and transferred for analysis without exposure to ambient air.

Powder X-ray diffraction (XRD) patterns were collected to verify the crystal structure using a Malvern PANalytical Empyrean diffractometer with Mo Kα radiation (λ = 0.71 Å) over a 2θ range of 5–35° with a step size of 0.016°. Rietveld refinement was performed using the FullProf software. *Operando* XRD measurements were carried out at the 3D XRS beamline at the Pohang Accelerator Laboratory (PAL), South Korea, using synchrotron radiation (λ = 0.688 Å). Diffraction patterns were recorded in transmission mode with a Mar345 image plate detector with an exposure time of 3 s. *Operando* XRD was conducted during the first charge/discharge at a current density of 40 mA g^{-1} within a voltage window of 2.3–4.7 V (*vs.* Li^+/Li). For ease of comparison with literature data, all diffraction angles were converted to those corresponding to Cu Kα radiation (λ = 1.54 Å). O K-edge soft X-ray absorption spectroscopy (sXAS) spectra were collected in total fluorescence yield (TFY) mode, which probes the bulk-averaged electronic structure and minimizes surface contamination artifacts, at the 4D-PES beamline at PAL. All XAS data were normalized using the Athena software [52]. Ni and Mn K-edge X-ray absorption spectra were collected at the 7D beamline of PAL in fluorescence mode, with the corresponding metal reference foils measured simultaneously for energy calibration. Data processing was performed using Athena. Fourier transforms of the EXAFS spectra were calculated with k^2 weighting over a k range of 3–11.5 $Å^{-1}$ using a Hanning window. The spectra were compared qualitatively without quantitative shell-by-shell fitting, and the displayed radial distances were not phase-corrected. Transmission electron microscopy (TEM) and atomic-resolution STEM-HAADF images were acquired using a Cs-corrected microscope (FEI, TITAN TM 80–300) operated at 200 kV at the Korea Institute of Science and Technology (KIST). The point resolution was better than 1 Å at the operating accelerating voltage. Images were recorded using a 4k × 4k CCD camera (Gatan Oneview 1095). The morphology and microstructure of the particles were examined using field-emission scanning electron microscopy (FE-SEM, Gemini SEM 560, ZEISS) at the National Center for Inter-University Research Facilities (NCIRF), Seoul National University. X-ray photoelectron spectroscopy (XPS) measurements were performed using an AXIS SUPRA spectrometer (Kratos Analytical) at NCIRF, Seoul National University. Additional XPS measurements (Figs. S5 and S7) were conducted using an AXIS Supra+ spectrometer (Kratos Analytical) at the Advanced Institutes of Convergence Technology (AICT). Binding energies were referenced to the C–C/C–H component of the C 1 s spectrum at 284.8 eV. The S 2*p* spectra were fitted using XPSPEAK 4.1 with a linear background and Gaussian–Lorentzian line shapes comprising 80% Gaussian and 20% Lorentzian contributions. Each S 2*p* doublet was constrained to an S $2p_{3/2}$:S $2p_{1/2}$ area ratio of 2:1, a spin–orbit splitting of 1.18 eV, and equal full widths at half maximum. Time-of-flight secondary ion mass spectrometry (ToF-SIMS) analyses were conducted in negative ion detection mode. Depth profiling was performed using a TOF.SIMS 5 instrument (ION-TOF GmbH, Germany) at NCIRF, Seoul National University, with Cs^+ sputtering and Bi_1^+ analysis beams. Additional mass spectra (Figs. S6 and S8) were collected using an M6 instrument at AICT. For comparison of the mass spectra, ion counts were normalized to the total detected ion counts in the corresponding spectrum, and the target-ion signals were reported as normalized intensities. Gas evolution was monitored using a gas-flow battery cell (GFBC, PDC TECH) interfaced with a DEMS manifold consisting of an Ar carrier-gas line, a mass-flow controller, and inlet/outlet capillaries. High-purity Ar (99.9999%) was supplied at 2.0 sccm, referenced to 0 °C and 1 atm. Before measurement, the cell and manifold were purged until a stable baseline was obtained. Cells were cycled between 2.3 and 4.7 V at 30 mA g^{-1} while the signals at $m/z = 32$, 44 and 40 were recorded. The O_2 and CO_2 signals were normalized to the simultaneously recorded Ar signal and corrected for the open-circuit baseline. Calibration factors relative to Ar were determined using a certified standard gas containing 100 μmol mol^{-1} each of O_2, CO_2 and CO in Ar under identical flow and pressure conditions. The calibration factors relating the Ar-normalized signals to the corresponding mole fractions were 2.86 for O_2 and 2.00 for CO_2. The calibrated concentrations were converted to molar evolution rates using the carrier molar flow of 89.2 μmol min^{-1} and normalized to the cathode active mass, yielding rates in μmol min^{-1} mg^{-1}. Cumulative O_2 and CO_2 evolution in μmol mg^{-1} was obtained by integrating the corresponding rates over the entire first charge–discharge cycle, from the start of charging to the end of discharge.

4.4. Computational details

DFT calculations were carried out using the Gaussian 16 software package and the Vienna Ab initio Simulation Package (VASP) [53]. Spin-unrestricted DFT calculations were performed using the Becke–Lee–Yang–Parr (B3LYP) hybrid exchange–correlation functional with the triple-zeta valence polarization (TZVP) basis set [54–58]. The optimized molecular structures of the additives and solvents were visualized using Avogadro [59]. To account for solvent effects, the EC/EMC/DMC (2:4:4 vol%) was modeled using an implicit dielectric environment with a dielectric constant of 21.468, consistent with previous reports. DFT calculations for the bulk and surface structures were conducted using VASP with projector-augmented-wave pseudopotentials and a plane-wave basis set [60]. The exchange–correlation energy was described using the Perdew–Burke–Ernzerhof functional within the generalized gradient approximation [61]. GGA+*U* was adopted to describe the localized Ni and Mn 3*d* states, with U values of 6.0 and 3.9 eV, respectively [62]. A $Li_{12}Ni_3Mn_{12}O_{36}$ surface model was constructed as a simplified layered Li–Ni–Mn–O slab containing Li in the transition-metal layers to investigate local oxygen stabilization in a reference configuration with nominal Ni^{4+}/Mn^{4+} states. The Ni:Mn ratio of 1:4 and the local cation arrangement were chosen to represent a Mn-rich surface environment in which oxygen atoms are coordinated to different combinations of Mn, Ni, and Li within the selected surface cell. The atomic arrangement is provided in Figs. S1 and S2. The model is not stoichiometrically equivalent to the experimental pristine $Li_{1.2}Ni_{0.2}Mn_{0.6}O_2$ composition. A 2 × 3 × 1 supercell was used, with a 6 × 3 × 3 k-point grid.

Surface calculations were performed using the (001) O-terminated LNM surface. The slab contained two transition-metal oxide layers with a substrate thickness of approximately 6.94 Å in a simulation cell of 23.68 Å along the surface-normal direction. For the SO_3-derived species-adsorbed structure before full delithiation, the minimum vacuum separation between periodic images was approximately 14.7 Å. No atomic layers were constrained, and all atoms were fully relaxed during structural optimization. One SO_3-derived species was introduced per 2 × 3

surface supercell, corresponding to a surface coverage of approximately 1.53 nm^{-2}.

The $Li_{12}Ni_3Mn_{12}O_{36}$ reference composition corresponds to nominal Ni^{4+}/Mn^{4+} states under the formal Li^+ and O^{2-} assignment. The model therefore approximates the nominal transition-metal oxidation states associated with partially delithiated $Li_{0.8}Ni_{0.2}Mn_{0.6}O_2$. At each modeled Li content, the bare and anchored surfaces have identical substrate compositions and Li-site occupancies. The Li-free computational limit was obtained by removing all 12 Li atoms. These states are used to evaluate oxygen electronic structure, adsorption, and oxygen-vacancy formation within the model.

All periodic calculations were performed with collinear spin polarization (ISPIN = 2). For the nominal Ni^{4+} model before full delithiation, initial magnetic moments of 0.0 and 3.0 μ_B were assigned to Ni and Mn, respectively. The nonzero Mn moments were initially aligned parallel. The same magnetic initialization scheme was applied to corresponding bare and SO_3-anchored structures at each Li content.

To evaluate the energetic favorability of S–O surface anchoring, adsorption energies of the SO_3-derived species were calculated on LNM surfaces before and after full delithiation. The isolated adsorbate used as the energy reference was an inorganic sulfur–oxygen model unit consisting of one sulfur atom and three oxygen atoms, with a net charge of 0 and a spin state of S = 0 (singlet). Its relationship to the proposed BS-derived organosulfonate precursor is limited to serving as an inorganic reference for the proposed S–O anchoring interaction. The SO_3-derived species was positioned to interact directly with the surface lattice oxygen, and the adsorption energy was calculated according to $E_{ads}=E_{(slab+adsorbate)}-E_{slab}-E_{adsorbate}$, where $E_{(slab+adsorbate)}$, E_{slab}, and $E_{adsorbate}$ represent the total energies of the adsorbed system, the corresponding LNM surface, and the isolated SO_3-derived species, respectively. A more negative E_{ads} indicates a more energetically favorable S–O-anchored configuration.

The influence of S–O anchoring on lattice-oxygen stability was further evaluated from oxygen-vacancy formation energies after full delithiation, with no Li atoms present in either substrate. For the SO_3-derived species-anchored surface, the LNM surface lattice oxygen directly involved in S–O anchoring was removed, while the corresponding lattice-oxygen site was removed from the bare LNM surface. The oxygen-vacancy formation energy was calculated according to $E_{vac}=E_{defective}+1/2\ E_{O2}-E_{perfect}$, where $E_{defective}$, $E_{perfect}$, and E_{O2} represent the total energies of the oxygen-deficient surface, the corresponding defect-free surface, and an isolated O_2 molecule, respectively. All structures containing an oxygen vacancy were fully relaxed after lattice-oxygen removal.

A plane-wave cutoff energy of 500 eV was used, and all atoms were relaxed until the residual forces were below 0.03 eV $Å^{-1}$. The Heyd–Scuseria–Ernzerhof (HSE06) hybrid functional was employed to obtain the projected density of states of Ni, Mn, and O. Crystal structures were rendered using VESTA software [63].

CRediT authorship contribution statement

Hyunjin Jang: Formal analysis, Investigation, Methodology, Validation, Visualization, Writing – original draft. **Seyeop Oh:** Writing – original draft, Visualization, Validation, Methodology, Investigation, Formal analysis, Conceptualization. **Hoseok Lee:** Software, Methodology, Formal analysis. **Hyunji Kweon:** Validation, Investigation. **Bonyoung Ku:** Validation, Investigation. **Myungeun Choi:** Methodology, Investigation. **Jihoe Lee:** Validation, Investigation. **Jinho Ahn:** Validation, Methodology. **Hyunyoung Park:** Validation, Investigation. **Myeong Hwan Lee:** Visualization, Validation. **Hyun-seung Kim:** Writing – review & editing, Supervision, Resources, Methodology. **Jongsoon Kim:** Writing – review & editing, Supervision, Resources, Project administration, Funding acquisition, Data curation, Conceptualization.

Declaration of Competing Interest

The authors declare that they have no known competing financial interests or personal relationships that could have appeared to influence the work reported in this paper.

Acknowledgements

This work was supported by the 2024 KRICT–SKKU Bilateral Research Program, funded by the Korea Research Institute of Chemical Technology and Sungkyunkwan University. This work was also supported by the National Research Foundation of Korea (NRF) under the National R&D Program, funded by the Ministry of Science and ICT of the Republic of Korea (RS-2024-00408156, 50%; RS-2024-00450728). In addition, this work was supported by the Technology Innovation Program (RS-2024-00427225, Development of manufacturing process technology for 3.7 V high voltage lithium iron manganese phosphate cathode) funded by the Ministry of Trade, Industry and Energy (MOTIE, Korea). Furthermore, this research was supported by a National Research Council of Science & Technology (NST) grant funded by the Korea government (MSIT) (No. GTL25092-303).

Appendix A. Supporting information

Supplementary data associated with this article can be found in the online version at doi:10.1016/j.nanoen.2026.112487.

Data Availability

Data will be made available on request.

References

[1] J. Ahn, J. Kang, M.K. Cho, H. Park, W. Ko, Y. Lee, H.S. Kim, Y.H. Jung, T.Y. Jeon, H. Kim, W.H. Ryu, J. Hong, J. Kim, Selective anionic redox and suppressed structural disordering enabling high-energy and long-life Li-rich layered-oxide cathode, Adv. Energy Mater. 11 (2021) 2102311, https://doi.org/10.1002/aenm.202102311.

[2] J. Lee, K. Nam, B. Ku, M. Choi, M.K. Cho, S.Y. Jung, J. Min, J. Ahn, Y. Lee, S.Y. Lee, D. Lee, Y.S. Cho, D.S. Kwon, J.K. Yoo, J. Kang, J. Kim, 2D phosphorene-decorated Ni-rich layered cathodes for high-power and high-energy Li-ion batteries, Adv. Funct. Mater. 36 (2026) 2511385, https://doi.org/10.1002/adfm.202511385.

[3] J. Ahn, H. Jang, H. Ahn, H. Kweon, S. Oh, S. Hwang, M.H. Lee, J. Hong, J. Kim, Co-free and Ni-minimized Li- and Mn-rich layered cathodes with suppressed structural disordering for high-performance and cost-effective LIBs, Adv. Energy Mater. 16 (2026) 2505121, https://doi.org/10.1002/aenm.202505121.

[4] J. Kim, H. Ahn, J. Ahn, H. Park, J. Hong, M.H. Lee, H. Park, J. Kim, Activation of oxygen redox by inhibited dynamic phase transition for high-energy Li-rich layered oxide cathode, Chem. Eng. J. 495 (2024) 153122, https://doi.org/10.1016/j.cej.2024.153122.

[5] T. Liu, J. Liu, L. Li, L. Yu, J. Diao, T. Zhou, S. Li, A. Dai, W. Zhao, S. Xu, Y. Ren, L. Wang, T. Wu, R. Qi, Y. Xiao, J. Zheng, W. Cha, R. Harder, I. Robinson, J. Wen, J. Lu, F. Pan, K. Amine, Origin of structural degradation in Li-rich layered oxide cathode, Nature 606 (2022) 305–312, https://doi.org/10.1038/s41586-022-04689-y.

[6] J. Zhang, Q. Zhang, D. Wong, N. Zhang, G. Ren, L. Gu, C. Schulz, L. He, Y. Yu, X. Liu, Addressing voltage decay in Li-rich cathodes by broadening the gap between metallic and anionic bands, Nat. Commun. 12 (2021) 3071, https://doi.org/10.1038/s41467-021-23365-9.

[7] K. McColl, S.W. Coles, P. Zarabadi-Poor, B.J. Morgan, M.S. Islam, Phase segregation and nanoconfined fluid O_2 in a lithium-rich oxide cathode, Nat. Mater. 23 (2024) 826–833, https://doi.org/10.1038/s41563-024-01873-5.

[8] M. Zhang, L. Qiu, W. Hua, Y. Song, Y. Deng, Z. Wu, Y. Zhu, B. Zhong, S. Chou, S. Dou, Y. Xiao, X. Guo, Formulating Local Environment of Oxygen Mitigates Voltage Hysteresis in Li-Rich Materials, Adv. Mater. 36 (2024) 2311814, https://doi.org/10.1002/adma.202311814.

[9] J.-J. Marie, R.A. House, G.J. Rees, A.W. Robertson, M. Jenkins, J. Chen, S. Agrestini, M. Garcia-Fernandez, K.-J. Zhou, P.G. Bruce, Trapped O_2 and the origin of voltage fade in layered Li-rich cathodes, Nat. Mater. 23 (2024) 818–825, https://doi.org/10.1038/s41563-024-01833-z.

[10] Q. Li, D. Ning, D. Wong, K. An, Y. Tang, D. Zhou, G. Schuck, Z. Chen, N. Zhang, X. Liu, Improving the oxygen redox reversibility of Li-rich battery cathode materials via Coulombic repulsive interactions strategy, Nat. Commun. 13 (2022) 1123, https://doi.org/10.1038/s41467-022-28793-9.

[11] H.Y. Jang, D. Eum, J. Cho, J. Lim, Y. Lee, J.H. Song, H. Park, B. Kim, D.H. Kim, S. P. Cho, S. Jo, J.H. Heo, S. Lee, J. Lim, K. Kang, Structurally robust lithium-rich

layered oxides for high-energy and long-lasting cathodes, Nat. Commun. 15 (2024) 1288, https://doi.org/10.1038/s41467-024-45490-x.
[12] T. Cui, J. Xu, X. Wang, L. Liu, Y. Xiang, H. Zhu, X. Li, Y. Fu, Highly reversible transition metal migration in superstructure-free Li-rich oxide boosting voltage stability and redox symmetry, Nat. Commun. 15 (2024) 4742, https://doi.org/10.1038/s41467-024-48890-1.
[13] X. Gao, B. Li, K. Kummer, A. Geondzhian, D.A. Aksyonov, R. Dedryvère, D. Foix, G. Rousse, M. Ben Yahia, M.L. Doublet, A.M. Abakumov, J.-M. Tarascon, Clarifying the origin of molecular O_2 in cathode oxides, Nat. Mater. 24 (2025) 743–752, https://doi.org/10.1038/s41563-025-02144-7.
[14] B. Wen, F.N. Sayed, W.M. Dose, J.K. Morzy, Y. Son, S. Nagendran, C. Ducati, C. P. Grey, M.F.L. De Volder, Surface reduction in lithium- and manganese-rich layered cathodes for lithium ion batteries drives voltage decay, J. Mater. Chem. A 10 (2022) 21941–21954, https://doi.org/10.1039/d2ta04876k.
[15] N.A. Shah, G.J. Páez Fajardo, H. Banerjee, G.C. Pandey, A.S. Menon, M. Ans, V. Majherova, G. Bree, S. Bolloju, D.C. Grinter, P. Ferrer, P.K. Thakur, T.-L. Lee, M. J. Loveridge, A.J. Morris, C.P. Grey, L.F.J. Piper, Nature of the Oxygen-Loss-Induced Rocksalt Layer and Its Impact on Capacity Fade in Ni-Rich Layered Oxide Cathodes, ACS Energy Lett. 10 (2025) 1313–1320, https://doi.org/10.1021/acsenergylett.5c00324.
[16] G. Lim, M.K. Cho, J. Choi, K.-J. Zhou, D. Shin, S. Jeon, M. Kwon, A.R. Jeon, J. Choi, S.S. Sohn, M. Lee, J. Hong, Decoupling capacity fade and voltage decay of Li-rich Mn-rich cathodes by tailoring surface reconstruction pathways, Energy Environ. Sci. 17 (2024) 9623–9634, https://doi.org/10.1039/d4ee02329c.
[17] H. Yu, Y. Cao, L. Chen, Y. Hu, X. Duan, S. Dai, C. Li, H. Jiang, Surface enrichment and diffusion enabling gradient-doping and coating of Ni-rich cathode toward Li-ion batteries, Nat. Commun. 12 (2021) 4564, https://doi.org/10.1038/s41467-021-24893-0.
[18] Y. Kim, H. Park, K. Shin, G. Henkelman, J.H. Warner, A. Manthiram, Rational Design of Coating Ions via Advantageous Surface Reconstruction in High-Nickel Layered Oxide Cathodes for Lithium-Ion Batteries, Adv. Energy Mater. 11 (2021) 2101112, https://doi.org/10.1002/aenm.202101112.
[19] G.-L. Xu, Q. Liu, K.K.S. Lau, Y. Liu, X. Liu, H. Gao, X. Zhou, M. Zhuang, Y. Ren, J. Li, M. Shao, M. Ouyang, F. Pan, Z. Chen, K. Amine, G. Chen, Building ultraconformal protective layers on both secondary and primary particles of layered lithium transition metal oxide cathodes, Nat. Energy 4 (2019) 484–494, https://doi.org/10.1038/s41560-019-0387-1.
[20] H.H. Sun, U.H. Kim, J.H. Park, S.W. Park, D.H. Seo, A. Heller, C.B. Mullins, C. S. Yoon, Y.K. Sun, Transition metal-doped Ni-rich layered cathode materials for durable Li-ion batteries, Nat. Commun. 12 (2021) 6552, https://doi.org/10.1038/s41467-021-26815-6.
[21] H. Li, P. Zhou, F. Liu, H. Li, F. Cheng, J. Chen, Stabilizing nickel-rich layered oxide cathodes by magnesium doping for rechargeable lithium-ion batteries, Chem. Sci. 10 (2019) 1374–1379, https://doi.org/10.1039/c8sc03385d.
[22] F. Wu, J. Dong, L. Chen, L. Bao, N. Li, D. Cao, Y. Lu, R. Xue, N. Liu, L. Wei, Z. Wang, S. Chen, Y. Su, High-voltage and high-safety nickel-rich layered cathode enabled by a self-reconstructive cathode/electrolyte interphase layer, Energy Storage Mater. 41 (2021) 495–504, https://doi.org/10.1016/j.ensm.2021.06.018.
[23] S. Tan, Z. Shadike, J. Li, X. Wang, Y. Yang, R. Lin, A. Cresce, J. Hu, A. Hunt, I. Waluyo, L. Ma, F. Monaco, P. Cloetens, J. Xiao, Y. Liu, X.-Q. Yang, K. Xu, E. Hu, Additive engineering for robust interphases to stabilize high-Ni layered structures at ultra-high voltage of 4.8 V, Nat. Energy 7 (2022) 484–494, https://doi.org/10.1038/s41560-022-01020-x.
[24] M. Choi, H. Choi, S. Park, W.M. Seong, Y. Lee, W. Ko, M.-K. Cho, J. Ahn, Y. Kong, J. Kim, Stabilized high-voltage operation of Co-free NMX cathode via CEI-controlling, Energy Storage Mater. 67 (2024) 103291, https://doi.org/10.1016/j.ensm.2024.103291.
[25] M. Choi, H.B. Lee, Y. Lee, H. Kweon, J. Ahn, B. Ku, J. Lee, S. Lee, J. Park, Y.M. Kim, J. Kim, Improving Cyclability and Structural Stability of Co-Free Layered Cathode by Controlling Porosity and Cracks in Secondary Particles for Low-Cost and High-Energy LIBs, Adv. Funct. Mater. 35 (2025) 2424880, https://doi.org/10.1002/adfm.202424880.
[26] Z. Li, Y. Wang, J. Wang, C. Wu, W. Wang, Y. Chen, C. Hu, K. Mo, T. Gao, Y.S. He, Z. Ren, Y. Zhang, X. Liu, N. Liu, L. Chen, K. Wu, C. Shen, Z.F. Ma, L. Li, Gradient-porous-structured Ni-rich layered oxide cathodes with high specific energy and cycle stability for lithium-ion batteries, Nat. Commun. 15 (2024) 10216, https://doi.org/10.1038/s41467-024-54637-9.
[27] C. Zhan, T. Wu, J. Lu, K. Amine, Dissolution, migration, and deposition of transition metal ions in Li-ion batteries exemplified by Mn-based cathodes – a critical review, Energy Environ. Sci. 11 (2018) 243–257, https://doi.org/10.1039/c7ee03122j.
[28] D. Cao, C. Tan, Y. Chen, Oxidative decomposition mechanisms of lithium carbonate on carbon substrates in lithium battery chemistries, Nat. Commun. 13 (2022) 4908, https://doi.org/10.1038/s41467-022-32557-w.
[29] D. Zhang, M. Liu, J. Ma, K. Yang, Z. Chen, K. Li, C. Zhang, Y. Wei, M. Zhou, P. Wang, Y. He, W. Lv, Q.H. Yang, F. Kang, Y.B. He, Lithium hexamethyldisilazide as electrolyte additive for efficient cycling of high-voltage non-aqueous lithium metal batteries, Nat. Commun. 13 (2022) 6966, https://doi.org/10.1038/s41467-022-34717-4.
[30] J. Xiao, N. Adelstein, Y. Bi, W. Bian, J. Cabana, C.L. Cobb, Y. Cui, S.J. Dillon, M. M. Doeff, S.M. Islam, K. Leung, M. Li, F. Lin, J. Liu, H. Luo, A.C. Marschilok, Y. S. Meng, Y. Qi, R. Sahore, K.G. Sprenger, R.C. Tenent, M.F. Toney, W. Tong, L. F. Wan, C. Wang, S.E. Weitzner, B. Wu, Y. Xu, Assessing cathode–electrolyte interphases in batteries, Nat. Energy 9 (2024) 1463–1473, https://doi.org/10.1038/s41560-024-01639-y.
[31] D.H. Seo, J. Lee, A. Urban, R. Malik, S. Kang, G. Ceder, The structural and chemical origin of the oxygen redox activity in layered and cation-disordered Li-excess cathode materials, Nat. Chem. 8 (2016) 692–697, https://doi.org/10.1038/nchem.2524.
[32] P. Rozier, J.-M. Tarascon, Review—Li-Rich Layered Oxide Cathodes for Next-Generation Li-Ion Batteries: Chances and Challenges, J. Electrochem. Soc. 162 (2015) A2490–A2499, https://doi.org/10.1149/2.0111514jes.
[33] G. Assat, J.-M. Tarascon, Fundamental understanding and practical challenges of anionic redox activity in Li-ion batteries, Nat. Energy 3 (2018) 373–386, https://doi.org/10.1038/s41560-018-0097-0.
[34] Z. Wang, Z. Wang, Z. He, A. Zhu, C. Li, T. Li, L. Mei, L. Chen, Nucleophilic Oxygen-Engineering Dual-Gradient Cathode–Electrolyte-Interphase for High-Voltage Lithium-Rich Manganese Oxide Cathodes, Angew. Chem. Int. Ed. 64 (2025) e14748, https://doi.org/10.1002/anie.202514748.
[35] A. Zhang, Z. Bi, E. Yang, T. Chen, X. Li, S. Liao, G. Wang, Y. Yu, X. Bao, Z.-S. Wu, Formulating Electrophilic Electrolyte for In Situ Stabilization of 4.8 V Li-Rich Batteries with 100% Initial Coulombic Efficiency, Angew. Chem. Int. Ed. 64 (2025) e202502603, https://doi.org/10.1002/anie.202502603.
[36] J. Heyd, G.E. Scuseria, Efficient hybrid density functional calculations in solids: assessment of the Heyd–Scuseria–Ernzerhof screened Coulomb hybrid functional, J. Chem. Phys. 121 (2004) 1187–1192, https://doi.org/10.1063/1.1760074.
[37] A.J. Garza, G.E. Scuseria, Predicting Band Gaps with Hybrid Density Functionals, J. Phys. Chem. Lett. 7 (2016) 4165–4170, https://doi.org/10.1021/acs.jpclett.6b01807.
[38] B. Ku, J. Ahn, H. Lee, H. Ahn, J. Lee, H. Kweon, M. Choi, H.-G. Jung, K. Ihm, E. Sim, J.-K. Yoo, J. Kim, Enhancing structural flexibility in P2-type Ni-Mn-based Na-layered cathodes for high power-capability and fast charging/discharging performance, Energy Storage Mater. 74 (2025) 103930, https://doi.org/10.1016/j.ensm.2024.103930.
[39] J. Lee, D.A. Kitchaev, D.H. Kwon, C.W. Lee, J.K. Papp, Y.S. Liu, Z. Lun, R. J. Clément, T. Shi, B.D. McCloskey, J. Guo, M. Balasubramanian, G. Ceder, Reversible Mn^{2+}/Mn^{4+} double redox in lithium-excess cathode materials, Nature 556 (2018) 185–190, https://doi.org/10.1038/s41586-018-0015-4.
[40] Y. Lee, H. Park, M.K. Cho, J. Ahn, W. Ko, J. Kang, Y.J. Choi, H. Kim, I. Park, W. H. Ryu, J. Hong, J. Kim, Li-Rich Mn–Mg Layered Oxide as a Novel Ni-/Co-Free Cathode, Adv. Funct. Mater. 32 (2022) 2204354, https://doi.org/10.1002/adfm.202204354.
[41] J. Hong, W.E. Gent, P. Xiao, K. Lim, D.H. Seo, J. Wu, P.M. Csernica, C.J. Takacs, D. Nordlund, C.J. Sun, K.H. Stone, D. Passarello, W. Yang, D. Prendergast, G. Ceder, M.F. Toney, W.C. Chueh, Metal-oxygen decoordination stabilizes anion redox in Li-rich oxides, Nat. Mater. 18 (2019) 256–265, https://doi.org/10.1038/s41563-018-0276-1.
[42] Y.S. Meng, G. Ceder, C.P. Grey, W.-S. Yoon, M. Jiang, J. Bréger, Y. Shao-Horn, Cation Ordering in Layered O3 $Li[Ni_xLi_{1/3-2x/3}Mn_{2/3-x/3}]O_2$ ($0 \le x \le 1/2$) Compounds, Chem. Mater. 17 (2005) 2386–2394, https://doi.org/10.1021/cm047779m.
[43] P. Hong, M. Xu, B. Liao, Y. Wu, N. Lin, Q. Huang, W. Li, Enhancing the Cycling Performance of High Voltage (4.5 V) $Li/LiNi_{0.5}Mn_{0.3}Co_{0.2}O_2$ Cell by Tailoring Sulfur-Derivative Cathode Passivation Film, J. Electrochem. Soc. 164 (2017) A2914–A2921, https://doi.org/10.1149/2.0181713jes.
[44] S. Wang, H. Guo, X. Li, Z. Wang, W. Peng, J. Wang, H. Duan, G. Li, G. Yan, How sulfur-containing additives stabilize Electrode/Electrolyte interface of high voltage Graphite/$LiCoO_2$ battery, Appl. Surf. Sci. 684 (2025) 161805, https://doi.org/10.1016/j.apsusc.2024.161805.
[45] S. Nanda, A. Manthiram, Delineating the Lithium–Electrolyte Interfacial Chemistry and the Dynamics of Lithium Deposition in Lithium–Sulfur Batteries, Adv. Energy Mater. 11 (2021) 2003293, https://doi.org/10.1002/aenm.202003293.
[46] X. Li, J. Huang, L. Yang, H.S. Chen, W.L. Song, S. Jiao, D. Fang, Quantifying the electrochemical kinetics of battery positive-electrode crystal facets, Nat. Commun. 16 (2025) 10229, https://doi.org/10.1038/s41467-025-65068-5.
[47] S. Tan, Y.J. Ji, Z.R. Zhang, Y. Yang, Recent progress in research on high-voltage electrolytes for lithium-ion batteries, ChemPhysChem 15 (2014) 1956–1969, https://doi.org/10.1002/cphc.201402175.
[48] J. Xu, M. Sun, R. Qiao, S.E. Renfrew, L. Ma, T. Wu, S. Hwang, D. Nordlund, D. Su, K. Amine, J. Lu, B.D. McCloskey, W. Yang, W. Tong, Elucidating anionic oxygen activity in lithium-rich layered oxides, Nat. Commun. 9 (2018) 947, https://doi.org/10.1038/s41467-018-03403-9.
[49] R.A. House, J.-J. Marie, M.A. Pérez-Osorio, G.J. Rees, E. Boivin, P.G. Bruce, The role of O_2 in O-redox cathodes for Li-ion batteries, Nat. Energy 6 (2021) 781–789, https://doi.org/10.1038/s41560-021-00780-2.
[50] T. Weigel, F. Schipper, E.M. Erickson, F.A. Susai, B. Markovsky, D. Aurbach, Structural and Electrochemical Aspects of $LiNi_{0.8}Co_{0.1}Mn_{0.1}O_2$ Cathode Materials Doped by Various Cations, ACS Energy Lett. 4 (2019) 508–516, https://doi.org/10.1021/acsenergylett.8b02302.
[51] W. Li, A. Dolocan, P. Oh, H. Celio, S. Park, J. Cho, A. Manthiram, Dynamic behaviour of interphases and its implication on high-energy-density cathode materials in lithium-ion batteries, Nat. Commun. 8 (2017) 14589, https://doi.org/10.1038/ncomms14589.
[52] B. Ravel, M. Newville, ATHENA and ARTEMIS: interactive graphical data analysis using IFEFFIT, Phys. Scr. T115 (2005) 1007–1010, https://doi.org/10.1238/Physica.Topical.115a01007.
[53] G. Kresse, J. Furthmüller, Efficiency of ab-initio total energy calculations for metals and semiconductors using a plane-wave basis set, Comput. Mater. Sci. 6 (1996) 15–50, https://doi.org/10.1016/0927-0256(96)00008-0.

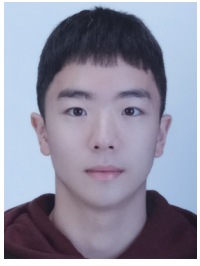
[54] A. Schäfer, C. Huber, R. Ahlrichs, Fully optimized contracted Gaussian basis sets of triple zeta valence quality for atoms Li to Kr, J. Chem. Phys. 100 (1994) 5829–5835, https://doi.org/10.1063/1.467146.
[55] A.D. Becke, Density-functional thermochemistry. III. The role of exact exchange, J. Chem. Phys. 98 (1993) 5648–5652, https://doi.org/10.1063/1.464913.
[56] C. Lee, W. Yang, R.G. Parr, Development of the Colle–Salvetti correlation-energy formula into a functional of the electron density, Phys. Rev. B 37 (1988) 785–789, https://doi.org/10.1103/physrevb.37.785.
[57] B. Klaumünzer, D. Kröner, P. Saalfrank, (TD-)DFT Calculation of Vibrational and Vibronic Spectra of Riboflavin in Solution, J. Phys. Chem. B 114 (2010) 10826–10834, https://doi.org/10.1021/jp100642c.
[58] P.J. Stephens, F.J. Devlin, C.F. Chabalowski, M.J. Frisch, Ab Initio Calculation of Vibrational Absorption and Circular Dichroism Spectra Using Density Functional Force Fields, J. Phys. Chem. 98 (1994) 11623–11627, https://doi.org/10.1021/j100096a001.
[59] M.D. Hanwell, D.E. Curtis, D.C. Lonie, T. Vandermeersch, E. Zurek, G.R. Hutchison, Avogadro: an advanced semantic chemical editor, visualization, and analysis platform, J. Cheminform. 4 (2012) 17, https://doi.org/10.1186/1758-2946-4-17.
[60] P.E. Blöchl, Projector augmented-wave method, Phys. Rev. B 50 (1994) 17953–17979, https://doi.org/10.1103/PhysRevB.50.17953.
[61] J.P. Perdew, K. Burke, M. Ernzerhof, Generalized Gradient Approximation Made Simple, Phys. Rev. Lett. 77 (1996) 3865–3868, https://doi.org/10.1103/PhysRevLett.77.3865.
[62] A. Jain, G. Hautier, S.P. Ong, C.J. Moore, C.C. Fischer, K.A. Persson, G. Ceder, Formation enthalpies by mixing GGA and GGA+U calculations, Phys. Rev. B 84 (2011) 045115, https://doi.org/10.1103/PhysRevB.84.045115.
[63] K. Momma, F. Izumi, VESTA: a three-dimensional visualization system for electronic and structural analysis, J. Appl. Crystallogr. 41 (2008) 653–658, https://doi.org/10.1107/s0021889808012016.



Hyunjin Jang has conducted research on lithium-ion batteries as an integrated M.S./Ph.D. student in the Department of Energy Science at Sungkyunkwan University (SKKU), Republic of Korea.



Seyeop Oh has conducted research on lithium-ion batteries as an M.S. student in the Department of Energy Science at Sungkyunkwan University (SKKU), Republic of Korea.



Hoseok Lee has conducted research on lithium-ion batteries as an integrated M.S./Ph.D. student in the Department of Future Energy Engineering at Sungkyunkwan University (SKKU), Republic of Korea.



Hyunji Kweon has conducted research on lithium-ion batteries as an M.S. student in the Department of Energy Science at Sungkyunkwan University (SKKU), Republic of Korea.



Bonyoung Ku has conducted research on lithium-ion batteries as an integrated M.S./Ph.D. student in the Department of Energy Science at Sungkyunkwan University (SKKU), Republic of Korea.



Myungeun Choi has conducted research on lithium-ion batteries as an integrated M.S./Ph.D. student in the Department of Energy Science at Sungkyunkwan University (SKKU), Republic of Korea.



Jihoe Lee has conducted research on lithium-ion batteries as an integrated M.S./Ph.D. student in the Department of Energy Science at Sungkyunkwan University (SKKU), Republic of Korea.



Jinho Ahn has conducted research on lithium-ion batteries as an integrated M.S./Ph.D. student in the Department of Energy Science at Sungkyunkwan University (SKKU), Republic of Korea.



Hyunyoung Park has conducted research on lithium-ion batteries as an integrated M.S./Ph.D. student in the Department of Energy Science at Sungkyunkwan University (SKKU), Republic of Korea.



Dr. Myeong Hwan Lee is a senior researcher at the Korea Research Institute of Chemical Technology (KRICT) and an adjunct professor at Sungkyunkwan University. He received his Ph.D. in materials science and engineering from Seoul National University in 2021 and conducted postdoctoral research at the University of California, San Diego, from 2021 to 2023. His research focuses on next-generation energy storage systems, including lithium-metal, sodium-ion, and aqueous batteries, with current emphasis on electrolyte and electrode design, interphase (SEI/CEI) engineering, and anionic-redox layered oxide cathodes.



Prof. Hyun-seung Kim is an associate professor in the Department of Battery Engineering at Sungkyunkwan University. He received his Ph.D. in chemical and biological engineering from Seoul National University. At the LG Chem Battery Research Institute, he worked on electrolyte development and battery degradation analysis and led the core technology development and mass-production implementation of the commercial electrolyte additive HS-02. He subsequently studied next-generation batteries at the Korea Electronics Technology Institute. His research focuses on degradation mechanisms and key materials for lithium-ion, sodium-ion, lithium-metal, and all-solid-state batteries through control of electrode–electrolyte interfacial reactions.



Prof. Jongsoon Kim is an associate professor in the Department of Energy Science at Sungkyunkwan University (SKKU). He received his Ph.D. in materials science and engineering from Seoul National University in 2014. Before joining SKKU in 2021, he was a senior researcher at the Korea Atomic Energy Research Institute and an assistant professor at Sejong University. His research focuses on advanced materials for lithium-ion, sodium-ion, and all-solid-state batteries. By integrating first-principles calculations, materials synthesis, and structural characterization, he aims to elucidate redox and degradation mechanisms and develop electrode and solid electrolyte materials with improved energy density, stability, and rate capability.